

B.P. Zeegers

Spontaneous Synchronization in Complex Networks

Bachelor's thesis

Supervisors:

dr. D. Garlaschelli (LION)
prof. dr. W.Th.F. den Hollander (MI)

August 20, 2015



Leiden Institute of Physics (LION)
Mathematical Institute (MI)

Leiden University

Abstract

Spontaneous synchronization of coupled oscillators is ubiquitous in biological and physical systems. Among the many attempts to model such behavior, the Kuramoto model has proven to be mathematically tractable yet sufficiently rich to capture this phenomenology. In the past three decades, numerous extensive studies have been devoted to the model. The first aim of this thesis is to review these works. In particular, we discuss the rich phenomenology of the Kuramoto model defined on complex networks, which has mainly been studied in the statistical physics literature. Moreover, we consider several rigorous results obtained in the mathematical literature concerning the synchronization behavior of the Kuramoto model with a mean-field coupling. As a second aim, we investigate a Kuramoto-like model defined on the hierarchical lattice. To this end, we provide a preliminary analysis for a renormalization program in order to rigorously describe the behavior of this model.

Contents

Abstract	iii
Contents	iv
1 Introduction	1
1.1 Motivation	1
1.2 The Kuramoto model	2
1.3 Thesis overview	3
2 Phenomenology of synchronization in the Kuramoto model	5
2.1 The mean-field Kuramoto model	5
2.1.1 Order parameter	6
2.1.2 Continuum limit	8
2.1.3 The analysis of Kuramoto	9
2.1.4 The bimodal case	11
2.1.5 Further work	13
2.2 The Kuramoto model on d -dimensional cubic lattices	15
2.3 The Kuramoto model on complex networks	16
2.3.1 Small-world networks	17
2.3.2 Scale-free networks	19
2.3.2.1 Onset of synchronization	20
2.3.2.2 Synchronization paths	22
2.3.3 Modular networks	24
3 Asymptotic behavior in the noisy mean-field Kuramoto model	27
3.1 Introduction	27
3.2 The model	28
3.3 McKean-Vlasov equation	29
3.3.1 Weak formulation	30
3.3.2 Strong formulation	31
3.4 Stationary solutions of the McKean-Vlasov equation	32
3.5 Limiting dynamics in the case of no disorder	34
3.6 Limiting dynamics in the case of symmetric disorder	35
3.6.1 Unimodal disorder	36
3.6.2 Binary disorder	37
4 A Kuramoto-like model on the hierarchical lattice	39
4.1 Introduction	39

4.2	The hierarchical group of order N	40
4.3	The model	41
4.4	Evolution of the block averages	44
4.4.1	Exact results	44
4.4.2	Expected behavior for $N \rightarrow \infty$	45
A	Numerical integration of stochastic differential equations (SDEs)	47
A.1	Informal interpretation of SDEs	47
A.2	Ito-Taylor approximation	48
A.3	Numerical integration schemes	50
B	Matlab code	53
B.1	Simulations in Chapter 2	53
B.2	Simulations in Chapter 3	55
B.3	Simulations in Chapter 4	56
	Bibliography	58

Chapter 1

Introduction

1.1 Motivation

To introduce the concept of spontaneous synchronization, let us first consider a paradigmatic example provided by fireflies living in the forests of Southeast Asia [41]. When the night falls, these fireflies start to flash *incoherently*, in which case their light pulses are uncoordinated. However, after a while these pulses become *synchronized*, so that eventually the whole population flashes in perfect unison. This surprising phenomenon has been under attention for centuries, but the first important clues for its explanation were found in the late 1960s [44]: It appears that each firefly isolated from the population flashes at its own *natural frequency*, but within the population somehow corrects its flashing rhythm to that of the other fireflies. These findings suggest that the fireflies can be viewed as a system of *coupled* oscillators. There is no central driving mechanism (such as a single firefly that conducts the flashing concert), and the fireflies reach a globally synchronized state only by their mutual interactions.

This kind of synchronization behavior is not limited to the flashing of fireflies, but in fact is ubiquitous in nature. Other biological examples include the simultaneous chirping of crickets [51], the heartbeat provided by pacemaker cells [36, 39] and neural synchronization phenomena in the human brain [1, 2]. Spontaneous synchronization also arises in a broad variety of contexts in physics, such as the flavor evolution of neutrinos [37], networks of microwave oscillators [57], power grids [2, 19], arrays of lasers [1, 29] and Josephson junctions [1, 53, 54]. There are many more examples, also in other disciplines such as climatology, economy and social sciences [2].

The omnipresence and complexity of spontaneous synchronization triggered scientists to search for a mathematical approach in order to understand the underlying principles. The first important work came from Winfree [55, 56], who recognized that spontaneous synchronization should be understood as a threshold process: If the coupling between the oscillators is sufficiently strong, then a macroscopic part of the population will freeze into synchrony. Although the model that Winfree proposed was difficult to

solve analytically [5], it inspired Kuramoto in 1975 to establish a more mathematically tractable model that captured the phenomenology [1].

1.2 The Kuramoto model

We consider a large population of N oscillators living in the unit circle $\mathbb{S} := \mathbb{R}/2\pi\mathbb{Z}$. Without any interactions, these oscillators rotate independently of each other around the unit circle at their natural frequencies:

$$\dot{\theta}_i(t) = \omega_i, \quad i = 1, \dots, N, \quad (1.1)$$

where for each oscillator i its phase (or angle) is denoted by θ_i and its natural frequency by ω_i . The frequencies ω_i are distributed according to a given probability density $\omega \mapsto g(\omega)$.

To capture spontaneous synchronization, Kuramoto extended (1.1) based on the findings of Winfree. The oscillators need to be coupled in some way, and both Winfree and Kuramoto realized that a mean-field coupling should be the easiest to work with [42]. In this case, all the oscillators interact with each other proportional to a strength that is the same for all pairs of oscillators (see Figure 1.1). Assuming this, Kuramoto proposed the following governing equations of what we shall from now on refer to as the *mean-field Kuramoto model* [30, 31]:

$$\dot{\theta}_i(t) = \omega_i + \frac{K}{N} \sum_{j=1}^N \sin(\theta_j(t) - \theta_i(t)), \quad i = 1, \dots, N, \quad (1.2)$$

where $K \geq 0$ is the coupling constant and the $1/N$ factor is incorporated to keep the model well-behaved in the limit $N \rightarrow \infty$.

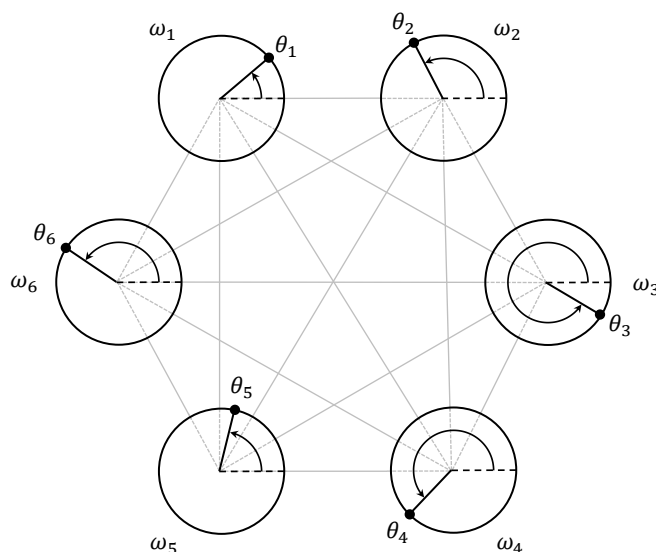


Figure 1.1: Interpretation of the mean-field Kuramoto model for $N = 6$. The complete graph visualizes the all-to-all coupling. Adapted from [34].

From (1.2) we see that each oscillator tends to rotate at its natural frequency, whereas the interaction term tends to make it rotate together with the other oscillators. In the case that the frequency density g is symmetric and unimodal (that is, with a single hump, for example a Gaussian), Kuramoto noticed that the model exhibits the temporal analog of a phase transition [42]: If the spread of the natural frequencies assigned to the population is too large compared to K , then the oscillators are not able to synchronize and rotate near their own frequencies. For increasing K , this remains the case until K exceeds a certain threshold K_c . Then a small fraction of synchronized oscillators starts to emerge and becomes of macroscopic size when K is increased even further. Hence, the critical coupling K_c separates the two regimes in which the system will be either in an incoherent state ($K < K_c$) or in a partially synchronized state ($K > K_c$).

Although the mean-field Kuramoto model proved to be sufficiently rich to display spontaneous synchronization, the assumption of an all-to-all coupling is hard to conceive for real-world systems [2]. By identifying oscillators with nodes and interactions with edges (as in Figure 1.1), it is possible to define the Kuramoto model on more general graphs, which introduces geometry into the model. Namely, given a graph with N nodes, the governing equations of the Kuramoto model on this graph are

$$\dot{\theta}_i(t) = \omega_i + \sigma \sum_{j \in \mathcal{V}(i)} \sin(\theta_j(t) - \theta_i(t)), \quad i = 1, \dots, N, \quad (1.3)$$

where $\mathcal{V}(i)$ is the set of nearest neighbors of node i and σ is the coupling constant with an appropriate scaling. For instance, to investigate the Kuramoto model on d -dimensional cubic lattices, a suitable scaling is $\sigma = \frac{K}{d}$ to keep the model well-behaved in the limit $d \rightarrow \infty$.

1.3 Thesis overview

The Kuramoto model offers exciting challenges both for physicists and mathematicians. In the past three decades, numerous extensive studies have been devoted to the model. Although it is impossible to accurately account for all these works, we will in Chapters 2 and 3 review the literature by considering groundbreaking results and illuminating examples.

Chapter 2 is focused on the phenomenology of synchronization that the Kuramoto model displays. This is first investigated for the mean-field Kuramoto model in Section 2.1, where several choices of the natural frequency distribution are considered. In particular, we follow Kuramoto's original analysis in identifying the critical coupling K_c for the case that the natural frequency distribution is symmetric and unimodal. To this end, (1.2) needs to be considered in the continuum limit $N \rightarrow \infty$. In Section 2.2 it is discussed that, compared to the mean-field model, the Kuramoto model on d -dimensional cubic lattices does not display macroscopic synchronization behavior.

On the other hand, defining (1.3) on complex networks yields a rich phenomenology, which has mainly been studied in the statistical physics literature. We discuss this in Section 2.3 for small-world networks, scale-free networks and modular networks.

However, most of the results discussed in Chapter 2 are not obtained on rigorous mathematical grounds. A precise understanding of the limiting behavior of the Kuramoto model as $N \rightarrow \infty$ is lacking in the literature, even for the mean-field Kuramoto model. Instead, the mathematical literature is largely concerned with the *noisy* mean-field Kuramoto model, of which the governing equations are obtained by adding white noise to (1.2). We review in Sections 2 and 3 of Chapter 3 a rigorous treatment for describing the behavior of this model as $N \rightarrow \infty$ with a partial differential McKean-Vlasov equation. With this equation we discuss in Sections 3.4-3.6 several mathematical results that can be identified with part of the synchronization phenomena considered in Section 2.1.

As an extension of the noisy mean-field Kuramoto model, we consider in Chapter 4 a Kuramoto-like model defined on the hierarchical lattice. A precise mathematical description of this lattice is given in Section 4.2, which defines a population that for each hierarchical level $k \in \mathbb{N}_0$ can be thought of as partitioned into so-called k -blocks of N^k oscillators. The dynamics on this lattice are defined in Section 4.3 and are such that equilibrium is reached sequentially in blocks of successive sizes. In Section 4.4 we give a preliminary analysis for a renormalization program to rigorously describe the behavior of the model in the *hierarchical mean-field limit* $N \rightarrow \infty$. We argue that in this limit the evolution of the oscillators in each block follows a noisy Kuramoto model at a time scale proportional to the size of the block.

Chapter 2

Phenomenology of synchronization in the Kuramoto model

In this chapter we review several synchronization phenomena that have been reported for the Kuramoto model. We focus on the mean-field Kuramoto model in Section 2.1, and in Sections 2.2 and 2.3 we consider the Kuramoto model defined on d -dimensional cubic lattices and complex networks, respectively.

2.1 The mean-field Kuramoto model

As explained in Section 1.2, the mean-field Kuramoto model consists of a large population of N oscillators living in the unit circle \mathbb{S} , each of them assigned a natural frequency ω_i drawn from some probability density $\omega \mapsto g(\omega)$, whose phases $\theta_i(t)$ evolve according to (1.2):

$$\dot{\theta}_i = \omega_i + \frac{K}{N} \sum_{j=1}^N \sin(\theta_j - \theta_i), \quad i = 1, \dots, N. \quad (2.1)$$

Without loss of generality we can take the mean of the natural frequency distribution to be zero, i.e.,

$$\Omega := \int_{-\infty}^{\infty} \omega g(\omega) d\omega = 0, \quad (2.2)$$

since redefining $\theta_i(t) \rightarrow \theta_i(t) + \Omega t$ leaves (2.1) invariant with effective natural frequencies $\omega_i - \Omega$. Indeed, this corresponds with putting ourselves in the frame rotating at frequency Ω .

To investigate the synchronization behavior of (2.1), we follow in the next three subsections the review article by Strogatz [42]. The first step is to introduce a so-called *order parameter* as the quantitative measure for synchronization in this model.

2.1.1 Order parameter

The complex-valued order parameter

$$re^{i\psi} = \frac{1}{N} \sum_{j=1}^N e^{i\theta_j} \quad (2.3)$$

is an empirical average that captures the collective rhythm produced by the population. In (2.3), $r(t)$ with $0 \leq r(t) \leq 1$ measures the phase coherence of the oscillators and $\psi(t)$ gives the average phase. For example, configurations in which the phases are spread more or less evenly over the circle correspond to $r \approx 0$ (see Figure 2.1a), whereas $r \approx 1$ indicates that the phases are close together (see Figure 2.1b).

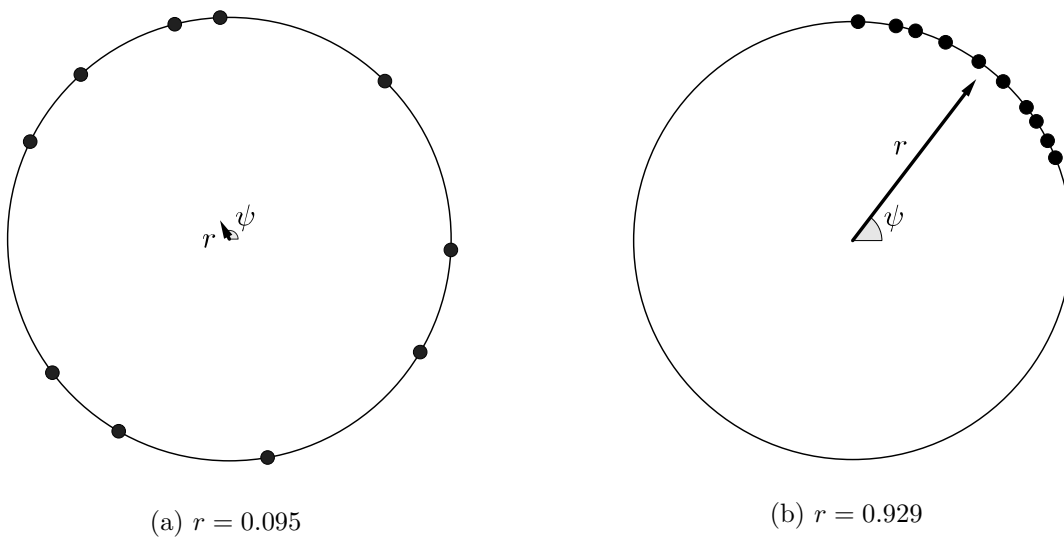


Figure 2.1: The phases of the oscillators are shown as points on the unit circle and the order parameter $re^{i\psi}$ is visualized by an arrow, having a length (a) $r \approx 0$ when the points are spread more or less uniformly over the circle; (b) $r \approx 1$ when the points are close together.

With the order parameter it is possible to write (2.1) in a more convenient form. To do so, we multiply both sides of (2.3) by $e^{-i\theta_i}$ ($i = 1, \dots, N$) to get

$$re^{i(\psi-\theta_i)} = \frac{1}{N} \sum_{j=1}^N e^{i(\theta_j-\theta_i)}, \quad i = 1, \dots, N. \quad (2.4)$$

The imaginary parts of (2.4) are

$$r \sin(\psi - \theta_i) = \frac{1}{N} \sum_{j=1}^N \sin(\theta_j - \theta_i), \quad i = 1, \dots, N, \quad (2.5)$$

which can be substituted into (2.1). In this way, (2.1) becomes

$$\dot{\theta}_i = \omega_i + Kr \sin(\psi - \theta_i), \quad i = 1, \dots, N, \quad (2.6)$$

exhibiting the mean-field nature of the model. Indeed, we have found that the oscillators are coupled merely via the order parameter. The interaction term in (2.6) tends to pull the phases θ_i towards the average phase ψ with a strength proportional to the phase coherence r . It is this proportionality that explains the underlying mechanism of spontaneous synchronization in the model. Namely, suppose that the oscillators become more coherent, resulting in an increase of r . Obviously, this leads to an increase of the coupling strength Kr , which in turn tends to make the population even more coherent.

Let us now look in more detail at how this synchronization process is revealed by the value of the phase coherence r . For this, we follow Kuramoto's assumptions, namely, we suppose that g is symmetric and unimodal around the zero frequency. The latter property means that $\omega \mapsto g(\omega)$ is strictly increasing on $(-\infty, 0]$ and strictly decreasing on $[0, \infty)$.¹ In this case, simulations carried out for (2.1) show that $r(t)$ has a typical evolution, exemplified by the simulations in Figure 2.2. For K smaller than a certain critical value K_c , the oscillators do not appear to feel the mutual interactions and just rotate around the unit circle near their natural frequencies. For each initial distribution of the phases, the oscillators therefore uniformly spread over the circle resulting in $r(t)$ decreasing to zero. On the other hand, for K larger than K_c the oscillators get divided in two groups. Those with natural frequencies sufficiently away from the center of g still rotate near their own frequencies, but the ones close to the center become phase-locked and rotate together with the average phase $\psi(t)$ at the mean frequency Ω (which is zero in the co-rotating frame). As a result, $r(t)$ settles to a value larger than zero, being independent of the initial distribution of the phases. This value becomes larger as K increases and tends to one as $K \rightarrow \infty$. The fluctuations of $r(t)$ in both the incoherent

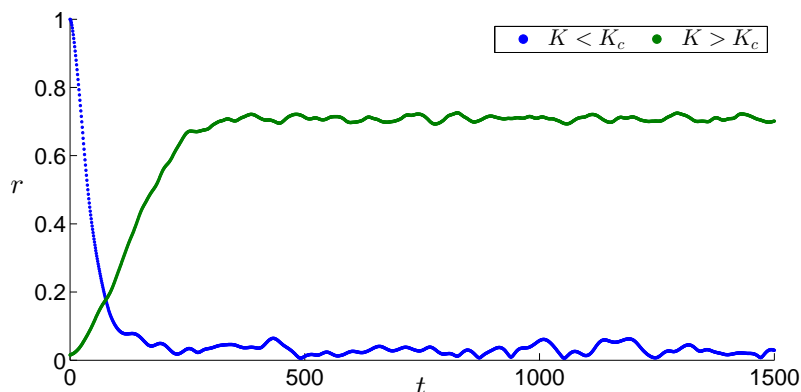


Figure 2.2: Typical evolution of $r(t)$ for the model (2.1) with $K < K_c$ and $K > K_c$. These simulation results are obtained with $N = 1000$ oscillators and g being the standard Gaussian density (so in this case $K_c \approx 1.6$ according to (2.20)), where the blue and green plot correspond to $K = 1$ and $K = 2$, respectively. As numerical integration scheme the Euler method is used, and the corresponding Matlab code is provided in Section 1 of Appendix B.

¹ This is the definition for a unimodal distribution that is used throughout the thesis. In this way, it is consistent with the meaning of unimodality in [34] (which is relevant in Subsection 3.6.1), although it is slightly stronger than the one used in [42], where a unimodal g needs to be nowhere decreasing on $(-\infty, 0]$ and nowhere increasing on $[0, \infty)$.

state and the partially synchronized states appear to scale as $N^{-1/2}$. In order to make mathematical statements about the relation between K and the limiting value of $r(t)$ as $t \rightarrow \infty$, it is useful to consider the model (2.1) in the continuum limit $N \rightarrow \infty$.

2.1.2 Continuum limit

In the limiting case of infinitely many oscillators, it is convenient to formulate the system in terms of densities. For this, we define $\rho(\theta, \omega, t)d\theta$ to be the fraction of oscillators with natural frequency ω and phase between θ and $\theta + d\theta$ at time t . Then, for each ω and t , the density $\rho(\theta, \omega, t)$ meets the periodicity condition

$$\rho(\theta + 2\pi, \omega, t) = \rho(\theta, \omega, t) \quad (2.7)$$

and the normalization condition

$$\int_0^{2\pi} \rho(\theta, \omega, t)d\theta = 1. \quad (2.8)$$

Since the number of oscillators with the same natural frequency should be conserved in time, ρ also needs to satisfy the continuity equation

$$\frac{\partial \rho}{\partial t} = -\frac{\partial}{\partial \theta}(\rho v), \quad (2.9)$$

which states that an increase of the density in a certain part of the circle involves a flow into this part from somewhere else. Here, $v(\theta, \omega, t)$ denotes the instantaneous velocity of an oscillator with phase θ and natural frequency ω , which we know from (2.6) to be equal to

$$v(\theta, \omega, t) = \omega + Kr(t) \sin(\psi(t) - \theta) \quad (2.10)$$

In (2.10), $r(t)$ and $\psi(t)$ are now determined from

$$r(t)e^{i\psi(t)} = \int_0^{2\pi} \int_{-\infty}^{\infty} e^{i\theta} \rho(\theta, \omega, t)g(\omega)d\omega d\theta, \quad (2.11)$$

which is the continuous counterpart of (2.3).²

Although the system defined by (2.7)-(2.11) seems to be the macroscopic equivalent of (2.1), note that we argued purely on physical grounds. This convergence of the finite N -model as $N \rightarrow \infty$ has not been rigorously established yet in the literature. However, in Section 3.3 we will review a rigorous mathematical proof of this result when white noise is added to (2.1).

In the light of the numerical results discussed in Subsection 2.1.1, we are interested in the stationary solutions of the system (2.7)-(2.11). Note that it has the trivial

² In fact, (2.9) represents a collection of equations, which are coupled via the order parameter (as is the case in (2.6)). This collection is for instance infinite when the set-theoretic support of g (i.e., the set $\text{supp}(g) = \{\omega \in \mathbb{R} : g(\omega) \neq 0\}$) is infinite (which is for example the case when g is a Gaussian density).

stationary solution

$$\rho(\theta, \omega) = \frac{1}{2\pi}, \quad r = 0, \quad (2.12)$$

independently of the choice we make for K and g . Obviously, this solution corresponds to the incoherent state as for instance shown in Figure 2.2. To find the stationary solutions that correspond to the partially synchronized states, it is illuminating to follow Kuramoto's original analysis in identifying the critical coupling K_c .

2.1.3 The analysis of Kuramoto

As discussed in Subsection 2.1.1, the oscillators in a partially synchronized state are split into two groups: one synchronized cluster of phase-locked oscillators rotating together with the average phase $\psi(t)$ at the mean frequency Ω , and one group of oscillators drifting relative to this cluster. Assuming r to be constant, Kuramoto found that the former group consists of those oscillators having natural frequencies $|\omega_i| \leq Kr$ and the latter group with those having frequencies $|\omega_i| > Kr$. In order to see why, we put ourselves in the frame rotating at frequency Ω . Then without loss of generality we can take ψ equal to zero, so that (2.6) reduces to

$$\dot{\theta}_i = \omega_i - Kr \sin(\theta_i), \quad i = 1, \dots, N. \quad (2.13)$$

The phase-locked oscillators satisfy $\dot{\theta}_i = 0$ in the rotating frame, and therefore stick to the phases θ_i given by

$$\omega_i = Kr \sin(\theta_i), \quad (2.14)$$

from which we indeed obtain $|\omega_i| \leq Kr$. On the other hand, the oscillators with frequencies $|\omega_i| > Kr$ cannot be locked and rotate erratically around the circle. Since r and ψ are supposed to be constant, Kuramoto assumed these drifting oscillators to form a stationary distribution on the circle. Because of (2.9), this assumption requires

$$\rho(\theta, \omega)v(\theta, \omega) = C(\omega) \quad (2.15)$$

for $|\omega| > Kr$, with $C(\omega)$ a constant (depending on ω). Hence, for each $K > K_c$ the stationary density of the partially synchronized state is

$$\rho(\theta, \omega) = \begin{cases} \delta(\theta - \arcsin(\frac{\omega}{Kr})), & |\omega| \leq Kr, \\ \frac{C(\omega)}{|\omega - Kr \sin \theta|}, & |\omega| > Kr. \end{cases} \quad (2.16)$$

Here, $C(\omega)$ is determined by the normalization condition (2.8), which gives

$$C(\omega) = \frac{1}{2\pi} \sqrt{\omega^2 - (Kr)^2}, \quad (2.17)$$

and is nonzero for $|\omega| > Kr$. In fact, since (2.15) with $C(\omega) = 0$ yields for $r > 0$ the delta function in (2.16), the stationary solutions of (2.9) with $r > 0$ are precisely those in (2.16).

Now, for each partially synchronized state, the corresponding stationary order parameter can be found by substituting (2.16) into (2.11). Note, however, that the solutions in (2.16) itself depend on the constant r . Therefore, in this way we obtain a so-called *self-consistency equation* for the order parameter. With g assumed to be symmetric, Kuramoto was able to reduce it to the form (see for instance [1, 42] for details)

$$r e^{i\psi} = Kr \int_{-\pi/2}^{\pi/2} \cos^2(\theta) g(Kr \sin \theta) d\theta. \quad (2.18)$$

Since we consider the case $r > 0$ and $\psi = 0$, we obtain from (2.18) that

$$1 = K \int_{-\pi/2}^{\pi/2} \cos^2(\theta) g(Kr \sin \theta) d\theta. \quad (2.19)$$

If we now let $r \downarrow 0$ in (2.19), we get Kuramoto's formula of the critical coupling:

$$K_c = \frac{2}{\pi g(0)}. \quad (2.20)$$

Furthermore, with an expansion of the integrand in (2.19) around $r = 0$, we can deduce the scaling law

$$r \sim \sqrt{\frac{16}{\pi K_c^4 [-g''(0)]}} (K - K_c)^{1/2} \quad (2.21)$$

as $K \downarrow K_c$. In particular, for g unimodal and sufficiently smooth around $\omega = 0$ (implying $g''(0) < 0$), the partially synchronized state bifurcates supercritically from the incoherent state for $K > K_c$, indicating a so-called *second-order* phase transition.

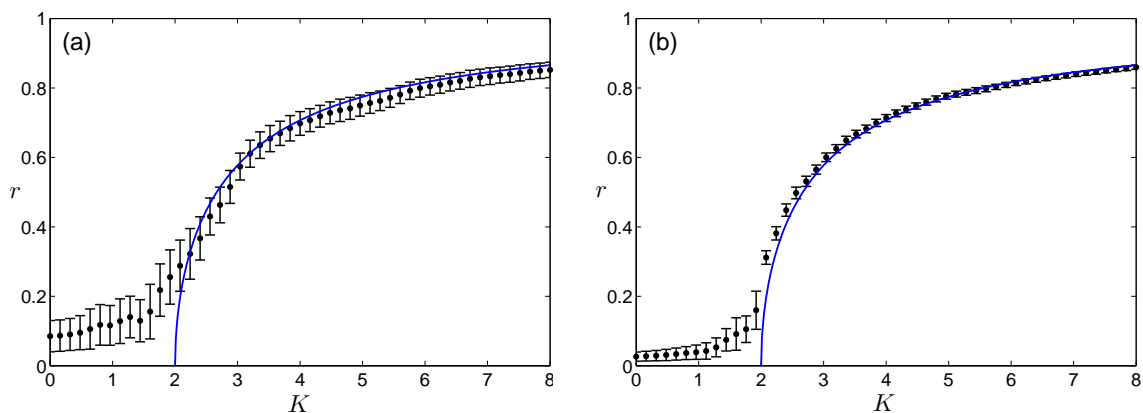


Figure 2.3: Phase diagram for the model (2.1) in the case of the Lorentzian frequency distribution (2.22) with $\Delta = 1$. Figures (a) and (b) show the simulation results obtained with $N = 100$ and $N = 1000$ oscillators, respectively, having natural frequencies that are the same for each evaluated K . In both figures, the blue plot corresponds to (2.23). For each investigated K , the corresponding r is the result from averaging over a time period after the system has settled into a stationary state, with error bars representing standard deviations. As numerical integration scheme the Euler method is used, and the corresponding Matlab code is provided in Section 1 of Appendix B.

As an example, we consider the particular case that g is Lorentzian (or Cauchy):

$$g(\omega) = \frac{\Delta}{\pi(\Delta^2 + \omega^2)}, \quad (2.22)$$

where $\Delta > 0$ is the scale parameter. The integral in (2.19) can then be evaluated explicitly, resulting in

$$r = \sqrt{1 - \frac{K_c}{K}} \quad (2.23)$$

for $K \geq K_c$, with $K_c = 2\Delta$. According to Figure 2.3, this result for the continuum limit model (2.7)-(2.11) coincides quite well with simulations carried out for the original model (2.1) with large but finite N .

2.1.4 The bimodal case

So far we have extensively discussed the phenomenology of the mean-field Kuramoto model when g is symmetric and unimodal. A natural question is to what extent these results still apply when g is shaped differently. An obvious choice is to consider a g that consists of two peaks. This *bimodal* frequency distribution has been investigated in the literature (see for instance [31], [14] and [35]), but the model proved to be considerably more difficult to analyze than in the unimodal setting.

We will restrict ourselves to the results presented in [35]. In this study, exact results have been obtained for the case that g is equal to the sum of two identical Lorentzian densities:

$$g(\omega) = \frac{\Delta}{2\pi} \left(\frac{1}{\Delta^2 + (\omega - \omega_0)^2} + \frac{1}{\Delta^2 + (\omega + \omega_0)^2} \right). \quad (2.24)$$

In (2.24), Δ is again the scale parameter of the two Lorentzians, and these are centered at $\pm\omega_0$ (see Figure 2.4). The analytical and numerical results of [35] are summarized in Figure 2.5, and show new phenomena compared to the unimodal case.

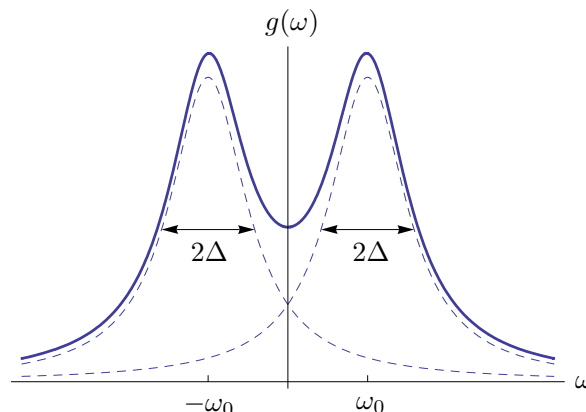


Figure 2.4: The bimodal distribution given by (2.24), being the sum of two identical Lorentzians. Adapted from [35].

For $\omega_0/\Delta < 1/\sqrt{3}$, we simply get the previously considered phase transition between incoherence and partial synchronization. Indeed, this is precisely the region for which the distribution (2.24) is unimodal, since the peaks are not far enough from each other relative to their widths to break unimodality.

In the region $1/\sqrt{3} < \omega_0/\Delta < 1$, the distribution still is hardly bimodal. However, what is new is that close to the phase transition boundary both the incoherent state and the partially synchronized state are stable. In this so-called *bistable* region, it depends on the initial distribution of the oscillators whether incoherence or synchronization prevails.

For $\omega_0/\Delta > 1$, the peaks of g are sufficiently separated such that stable *standing waves* emerge in the phase diagram. In these states, the population is split into two counter-rotating clusters of oscillators. This happens in the intermediate region where the coupling is strong enough to lock oscillators with frequencies around the same peak of g , but too weak to lock the two clusters. As we see from Figure 2.5, the standing waves coexist with partially synchronized states for $1 < \omega_0/\Delta < 1.18$, and this bistability has fully disappeared for $\omega_0/\Delta > 1.81$.

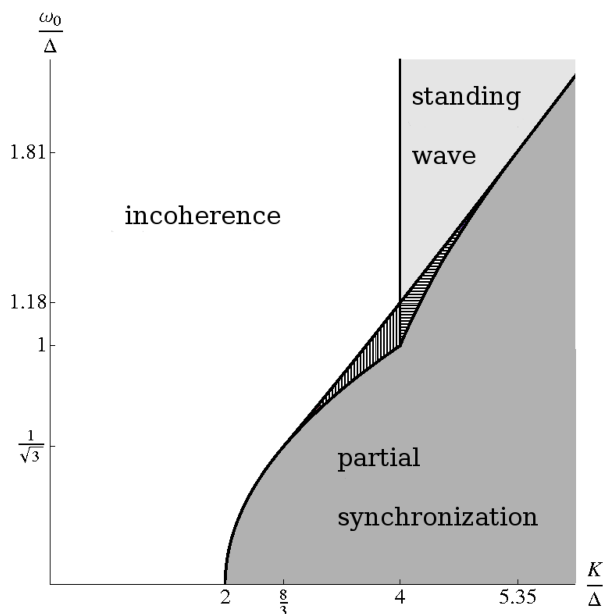


Figure 2.5: Phase diagram for the mean-field Kuramoto model with g given by (2.24). It consists of regions of incoherence (white), partial synchronization (dark gray), standing waves (light gray) and bistability, where in the last case partially synchronized states coexist either with incoherent states (vertical lines) or with standing waves (horizontal lines). From [35].

The question how the states in Figure 2.5 bifurcate from each is more delicate than in the unimodal setting. A detailed bifurcation analysis can be found in [35], where in addition similar results have been obtained for the case that g is a sum of two identical Gaussians.

2.1.5 Further work

Below, we review some other interesting phenomena observed in the mean-field Kuramoto model, and we discuss several open problems. For a more complete review of the literature on this subject we refer to [1, 42] and references therein.

Following the analysis of Kuramoto, we have seen that when the frequency distribution is chosen to be symmetric and unimodal, the mean-field Kuramoto model exhibits a second-order phase transition. In this case the partially synchronized state bifurcates continuously from the incoherent state (see Figure 2.3). For uniform frequency distributions, however, it has been found [38, 48, 49] that this transition occurs discontinuously (a so-called *first-order* phase transition). Specifically, with

$$g(\omega) = \begin{cases} \frac{1}{2\gamma}, & |\omega| \leq \gamma, \\ 0, & |\omega| > \gamma, \end{cases} \quad (2.25)$$

the value of r takes a jump from zero to $r_c = \pi/4$ when K exceeds $K_c = 4\gamma/\pi$ (which coincides with Kuramoto's critical coupling (2.20) using (2.25)), as is shown in Figure 2.6. Furthermore, instead of a square-root scaling law as in (2.21), it has been found in [38] that in this case $r - r_c \sim (K - K_c)^{2/3}$ as $K \downarrow K_c$. The phenomenon exemplified by Figure 2.6 is the first discovered example of so-called *explosive synchronization* [58].

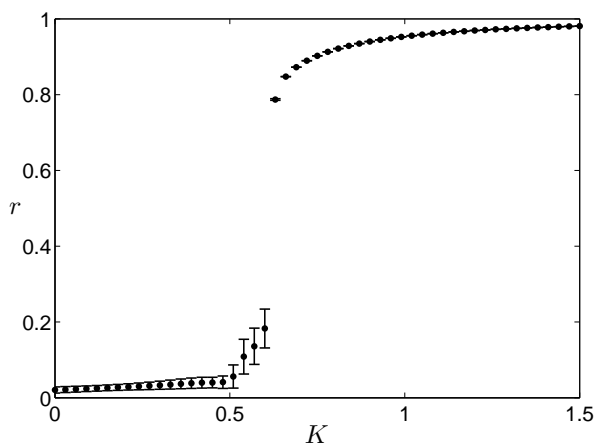


Figure 2.6: Phase diagram for the model (2.1) with $N = 2000$ oscillators, having natural frequencies distributed according to (2.25) with $\gamma = 1/2$ that are the same for each evaluated K . Each obtained r is the result from averaging over a time period after the system has settled into a stationary state, with error bars representing standard deviations. As numerical integration scheme the Euler method is used, and the corresponding Matlab code is provided in Section 1 of Appendix B.

As already pointed out, a major open problem concerns the limiting behavior of the mean-field Kuramoto model (2.1) as $N \rightarrow \infty$. Although the use of the continuum model (2.7)-(2.11) in Kuramoto's analysis seems to be justified by simulations (as in Figure 2.3), paradoxical issues arise when considering the order of the limits $N \rightarrow \infty$ and $t \rightarrow \infty$ applied to (2.1) [1]. For that reason, attempts have been made to investigate

the limiting dynamics of (2.1) for finite N , and then to prove convergence results as $N \rightarrow \infty$ [42] (that is, reversing the order of the limits $N \rightarrow \infty$ and $t \rightarrow \infty$ with respect to Kuramoto's analysis). Using simulations and physical arguments, results have been obtained that indeed confirm the scaling $N^{-1/2}$ as $N \rightarrow \infty$ for the fluctuations of the order parameter [1]. However, if K is close to K_c , then the scaling becomes larger. In particular, Daido found for unimodal frequency distributions that the fluctuations scale like $[(K_c - K)N]^{-1/2}$ as $K \uparrow K_c$ and like $(K - K_c)^{-1/8}N^{-1/2}$ as $K \downarrow K_c$ [1, 18]. In spite of these results, no mathematically rigorous convergence results have been obtained for the mean-field Kuramoto model.

On the other hand, a rigorous treatment of the convergence problem has been established for the *noisy* mean-field Kuramoto model, which we consider in Chapter 3. The governing equations (3.1) of this model are obtained by adding white noise to (2.1). In Section 3.3 we review the convergence results of the noisy model as $N \rightarrow \infty$, in which case the behavior of the system is described by the McKean-Vlasov equation (or Fokker-Planck equation)

$$\frac{\partial p_t(\theta, \omega)}{\partial t} = -\frac{\partial}{\partial \theta} (p_t(\theta, \omega)v_t(\theta, \omega)) + D\frac{\partial^2 p_t(\theta, \omega)}{\partial \theta^2}, \quad (2.26)$$

which coincides with the continuum equation given by (2.9)-(2.11) up to the diffusive term with strength $D > 0$. However, as remarked in [1], a fundamental difference is that ρ in (2.9) is a distribution, whereas p in (2.26) is a smooth function (see Proposition 3.4). This allows for a more rigorous analysis of the model, and much of the mathematical literature is concerned with this setting. We discuss the asymptotic dynamics of (2.26) in Sections 3.4-3.6. To use this for the mean-field Kuramoto model without noise, the behavior of the noisy model as $D \downarrow 0$ needs to be considered.

Another important open problem concerns the stability of the stationary states of (2.1) [1, 42]. Although it appears from simulations (as in Figure 2.3) that in the unimodal setting the global attractor is either the incoherent state ($K < K_c$) or the partially synchronized state ($K > K_c$), this has not yet rigorously proven. However, rigorous results concerning the local stability of the incoherent state have been obtained by Strogatz and Mirollo in [47]. By linearizing the McKean-Vlasov equation (2.26) about $p = \frac{1}{2\pi}$, they showed that in the unimodal setting the incoherent state is linearly stable below threshold and unstable above it. From this, they obtained that the model without noise (i.e., $D = 0$) has a pathological stability character [47]: Whereas the incoherent state is also in this case unstable above threshold, it becomes *neutrally* stable whenever $K < K_c$. Therefore, adding infinitesimal noise to (2.1) changes the stability properties of the model considerably. The problem of proving that the partially synchronized states are locally stable turns out to be much more complicated [42, 47].

2.2 The Kuramoto model on d -dimensional cubic lattices

In the mean-field Kuramoto model each oscillator is coupled to all the others with the same strength. The lack of geometry makes this complete graph setting relatively easy to treat analytically, but for many real-world systems it could be considered as too much of a simplification. In this section we add geometry to the model in the form of local interactions by considering d -dimensional cubic lattices. In this case, the governing equations are

$$\dot{\theta}_i = \omega_i + \frac{K}{d} \sum_{j \in \mathcal{V}(i)} \sin(\theta_j - \theta_i), \quad i = 1, \dots, N = L^d, \quad (2.27)$$

where $\mathcal{V}(i)$ is the set of the nearest neighbors of node i and the natural frequencies ω_i are again distributed according to some probability density $\omega \mapsto g(\omega)$. Since the number of elements in $\mathcal{V}(i)$ is proportional to d , we have now scaled the coupling strength K by d to keep the model well-behaved as $d \rightarrow \infty$.

As opposed to the mean-field Kuramoto model, the synchronization behavior of the model in (2.27) cannot be investigated by solving for its governing equations, since this appears to be a hopeless task [1]. Yet, it has been found [1] that synchronization in the form of phase coherence (as measured by the modulus r of the order parameter defined in (2.3)) does not occur in the lattices except when $K \sim N \rightarrow \infty$. Phase coherence, however, is a relatively strong form of synchronization, since it requires that all phases θ_i are accumulated around a single value, and also their velocities $\dot{\theta}_i$. In several studies [17, 45, 46] the synchronization behavior of (2.27) is therefore investigated by considering so-called *entrainment* or *clustering*. This refers to the case that part of the oscillators shares a common average frequency $\tilde{\omega}_i$ defined by³

$$\tilde{\omega}_i = \lim_{t \rightarrow \infty} \frac{\theta_i(t)}{t}, \quad (2.28)$$

but within this group of oscillators (called a *cluster* in the rest of this section) the phases could be entirely different. Though it is not known under what conditions the limit in (2.28) exists, it is clear that if it does not exist, then no form of synchronization is possible [1, 46].

As an example of clustering, we consider the simulation results from [45] shown in Figure 2.7. Pictured is the formation of clusters in a finite two-dimensional lattice, where the difference in shades of grey of the sites correspond to the difference in the oscillators' averaged frequencies (defined as in (2.28) but for finite t). At the start of the simulation, each oscillator runs at its natural frequency (Figure 2.7a). Then, by the influence of the coupling, clusters gradually arise and become sharply defined around $t = 10^4$ (Figure 2.7b), which for the simulation turns out to be the asymptotic steady state.

³In (2.28), the phase $\theta_i(t)$ should be considered as an element of \mathbb{R} instead of \mathbb{S} .

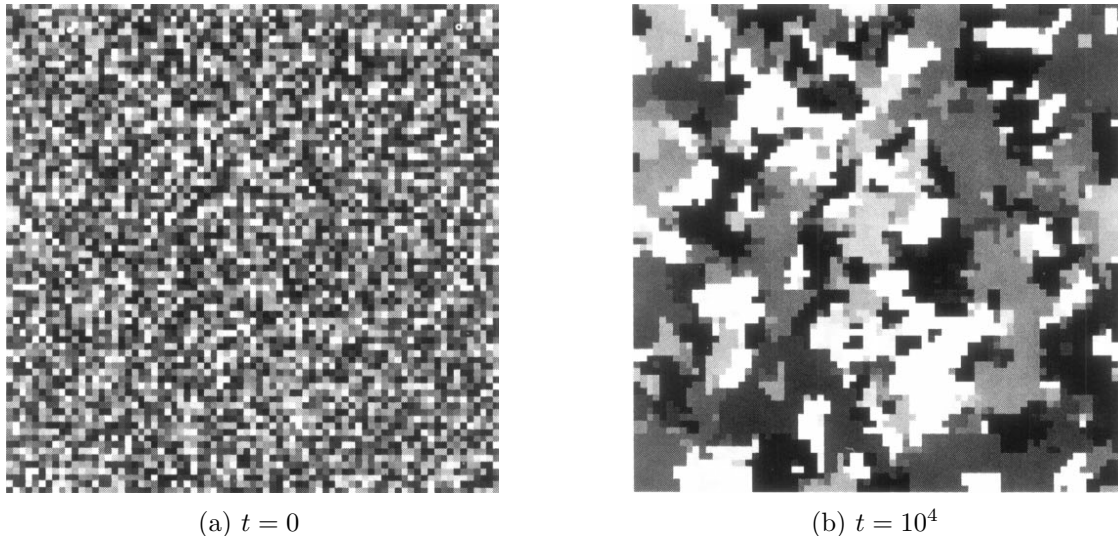


Figure 2.7: Part of the results from [45] obtained by simulating (2.27) with $K = 0.5$, $d = 2$, $L = 75$, g the uniform probability density on $[0, 1]$ and $\theta_i(0) = 0$ ($i = 1, \dots, N$) the initial condition. Visualized are the local frequencies in the lattice, indicated by the grey levels and increasing from white to black. (a) The natural frequencies ω_i of the oscillators are pictured. (b) The frequencies $\tilde{\omega}_i$, defined as in (2.28) but for $t = 10^4$, are pictured.

The compact clusters in Figure 2.7, or droplet-shaped clusters as they are called in [45], appear to be a finite-size effect of the lattice. In fact, such clusters do not develop in the model (2.27) as the population size diverges. More precisely, for any $d \geq 1$, the probability $P(N, K, d, \alpha)$ that (2.27) has a solution for which at least one d -dimensional cubical cluster of size αN ($0 < \alpha \leq 1$) arises, satisfies ([45], see also [46])

$$P(N, K, d, \alpha) \sim N e^{-cN}, \quad N \rightarrow \infty, \quad (2.29)$$

where $c > 0$ is a constant. Therefore, this probability rapidly vanishes in the limit of large N . In particular, (2.29) shows that in the model (2.27) with $d = 1$ no cluster of size $O(N)$ can arise as $N \rightarrow \infty$, since in this case every cluster is a line segment and therefore ‘cubical’. Moreover, in the case that $d > 1$, it follows from (2.29) that if a macroscopic cluster exists, it must have a noncompact structure, or as it is put in [45], such a cluster must be “sponge-like, riddled with holes”.

2.3 The Kuramoto model on complex networks

In this section we review the physical literature concerned with the synchronization behavior of the Kuramoto model on complex networks. For this, we distinguish between small-world networks, scale-free networks and modular networks, and we show that these cases cover a rich phenomenology. We explain the associated network theory, but we refer to [13, 43] for more extensive reviews of the theory of complex networks.

2.3.1 Small-world networks

Many real-world networks share a common property known as the *small-world* effect. This means that although most nodes have a degree that is much smaller than the size of the network, these can be reached from the other nodes via a small number of links. Typically for such a network, the average path length L (defined as the average number of links in the shortest path between two nodes) is at most proportional to the logarithm of the size N of the network, i.e. $L = O(\log N)$ [13].

Perhaps the most popular small-world networks are the ones that appear in the Watts-Strogatz model [52]. In this model, as starting point a ring lattice of N nodes is considered, in which each node is directly linked to its k nearest neighbors. For a given $p \in [0, 1]$, each link in this lattice is then randomly rewired with probability p , without changing the number of nodes or links in the network (see Figure 2.8). It is assumed that $N \gg k \gg \ln(N) \gg 1$, because the obtained networks are required to be connected (which is ensured by $k \gg \ln(N)$ according to [8]) and not to be too dense (i.e., $N \gg k$) in order to display the small-world effect. With the rewiring procedure, Watts and Strogatz found that when p is increased from zero (the regular case) to one (the random case), the corresponding average path length $L(p)$ of the resulting network rapidly drops for $0 < p \ll 1$ and, compared to $L(0)$, remains small for larger p . The reason for this drop is that for small p , the few rewired links serve as short cuts in reaching nodes from the others. So like the random graph, the small-world networks in the region $0 < p \ll 1$ have a small $L(p)$, but still are highly clustered, like the regular lattice.

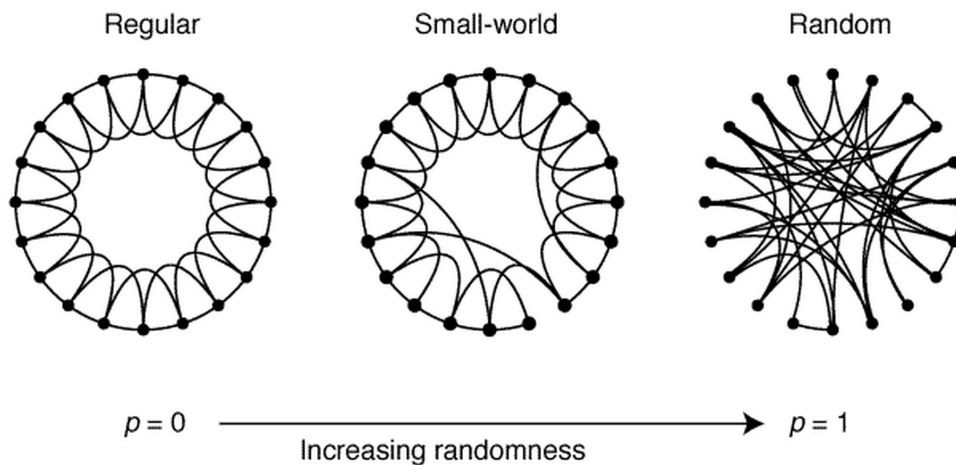


Figure 2.8: The rewiring procedure in the Watts-Strogatz model as a function of p , illustrated for a ring lattice with $N = 20$ and $k = 4$. From [52].

For defining the Kuramoto model on the small-world networks in the Watts-Strogatz model, we need a suitable scaling for the coupling strength in order to properly compare for different choices of the initial lattice. Since in the rewiring process links are reconnected to nodes chosen uniformly at random, we know that starting with a ring lattice with N nodes of degree k yields networks with average degree equal to k .

Therefore, we consider the governing equations

$$\dot{\theta}_i = \omega_i + \frac{K}{k} \sum_{j \in \mathcal{V}(i)} \sin(\theta_j - \theta_i), \quad i = 1, \dots, N \quad (2.30)$$

on a network generated with the Watts-Strogatz model, where $\mathcal{V}(i)$ again denotes the set of the nearest neighbors of node i and the natural frequencies ω_i are again distributed according to some probability density $\omega \mapsto g(\omega)$.

For the case that g is the standard Gaussian density, the phase diagram of (2.30) is shown in Figure 2.9 and is based on numerical results reported in [27]. In this study, the degree of the nodes in the initial ring lattice is for convenience taken to be $k = 6$. Moreover, different sizes of the initial lattice (up to $N = 3200$) are used, over which the results have been averaged. As Figure 2.9 indicates, there is no finite critical coupling for the Kuramoto model on the regular lattice ($p = 0$), which means that in this case no synchronization in the form of phase coherence can occur. (This was to be expected from the fact that global synchronization in d -dimensional cubic lattices occurs only as $K \sim N \rightarrow \infty$, as we discussed in Section 2.2.) On the other hand, $K_c(p)$ is finite for $p > 0$ and rapidly drops with the introduction of only a small number of shortcuts. In these small-world networks, information flows quickly through all the nodes as implied by the small average path length $L(p)$, and the time for the system to reach a synchronized state decreases as p increases [27]. Although the small-world networks have only a small number of links compared to the mean-field case, the corresponding critical couplings $K_c(p)$ are relatively close to the mean-field critical coupling $K_c = 2/\pi g(0) \approx 1.60$ of (2.20), which can be recovered by letting k increase [2]. Furthermore, the results in [27] indicate that the synchronized state bifurcates from the incoherent state following a square-root scaling law, which is also the case in (2.21) for the mean-field model.

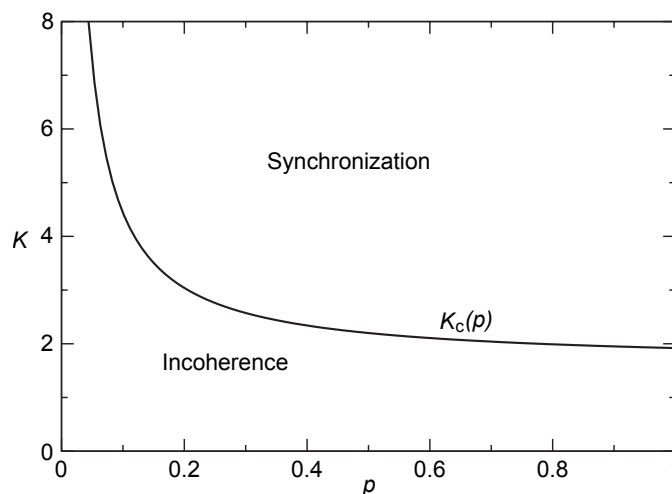


Figure 2.9: Phase diagram of (2.30), derived from the numerical results in [27] with $k = 6$ and g the standard Gaussian density, and with various sizes of the initial lattice up to $N = 3200$. The phase transition boundary is approximately $K_c(p) = 1.64 + 0.28p^{-1}$, which is obtained by averaging over the used network sizes, each for which 100 different realizations of the Watts-Strogatz model are considered, with different natural frequencies. Adapted from [6].

2.3.2 Scale-free networks

Even though the Watts-Strogatz model is able to produce networks with small-world properties, these networks are typically very different from real-world networks. An important difference concerns the degree distribution $P(k)$ of the networks. Random graphs (like the one in Figure 2.8) usually have a degree distribution with an exponential tail. For instance, the Erdős-Rényi random graph, in which each pair in N nodes is independently connected with probability p (or not, with probability $1 - p$), has a binomial degree distribution:

$$P(k) = \binom{N-1}{k} p^k (1-p)^{N-1-k}, \quad k = 0, 1, \dots, N-1. \quad (2.31)$$

However, the degree distribution of many real-networks roughly follows a power law:

$$P(k) \sim k^{-\gamma}, \quad (2.32)$$

where γ is a constant, typically in the range $2 < \gamma < 3$. Such networks are referred to as *scale-free*. Since distributions of the form (2.32) are heavy-tailed, some of the nodes in a scale-free network have a lot more connections than others (see Figure 2.10). These *hubs* connect many parts of the network to each other, giving the scale-free network its small-world properties. In fact, whereas scale-free networks with degree distribution (2.32) for $\gamma > 3$ have an average path length $L \sim \log N$, the case $2 < \gamma < 3$ corresponds to $L \sim \log \log N$, known as the *ultra small-world* effect [11].

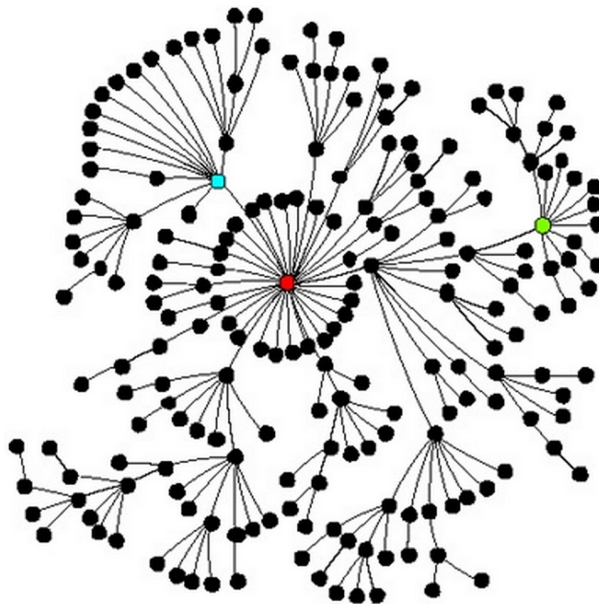


Figure 2.10: Example of a scale-free network. A majority of the nodes is poorly connected, and a minority has relatively many connections (the hubs). The red, blue and green node are the three nodes with the most connections (33, 12 and 11 links, respectively). From [43].

In the following we will investigate how these structural properties influence the synchronization behavior when we define the Kuramoto model on scale-free networks as

$$\dot{\theta}_i = \omega_i + \sigma \sum_{j \in \mathcal{V}(i)} \sin(\theta_j - \theta_i), \quad i = 1, \dots, N, \quad (2.33)$$

where σ is the coupling strength with an appropriate scaling, and the natural frequencies ω_i are again distributed according to some probability density $\omega \mapsto g(\omega)$. Dividing by the average degree of the network serves as a suitable scaling for (2.30), but this is not the case for (2.33). Due to the presence of hubs, this choice gives problems for scale-free networks as $N \rightarrow \infty$. According to [2], the only appropriate choice is $\sigma = K/k_{\max}$, where k_{\max} denotes the degree of the node with the most connections in the network.

2.3.2.1 Onset of synchronization

Like in Subsection 2.1.3, we investigate for (2.33) the onset of synchronization as measured by the order parameter

$$r e^{i\psi} = \frac{1}{N} \sum_{j=1}^N e^{i\theta_j}. \quad (2.34)$$

Since we are working on a scale-free network, we cannot write (2.33) directly in terms of (2.34). Therefore, we follow [32] in making the assumption that the effective field between each pair of coupled oscillators has the same magnitude, so that (2.33) simplifies to

$$\dot{\theta}_i = \omega_i + \sigma k_i \bar{r} \sin(\bar{\psi} - \theta_i), \quad i = 1, \dots, N, \quad (2.35)$$

with the weighted order parameter

$$\bar{r} e^{i\bar{\psi}} = \frac{\sum_{j=1}^N k_j e^{i\theta_j}}{\sum_{j=1}^N k_j}. \quad (2.36)$$

For the case that g is the standard Gaussian density, it has been shown in [32] that the emergence of nonzero r and \bar{r} — describing for (2.35) the phase transition from incoherence to synchronization — occur at the same threshold σ_c . This suggests that for more general g we can determine the onset of synchronization as measured by (2.34) by proceeding in the same kind of way as in Section 2.1, now with (2.35) and (2.36) instead of (2.6) and (2.3). To this end, we follow [28].

Again, it is convenient to formulate the system under consideration in the continuum limit $N \rightarrow \infty$. For this, we define $\rho(\theta, \omega, k, t) d\theta$ to be the fraction of oscillators with natural frequency ω and phase between θ and $\theta + d\theta$ at time t , and for which the corresponding nodes have degree k in the scale-free network. Then, for each ω , k and

t , the density $\rho(\theta, \omega, k, t)$ meets the periodicity condition

$$\rho(\theta + 2\pi, \omega, k, t) = \rho(\theta, \omega, k, t) \quad (2.37)$$

and the normalization condition

$$\int_0^{2\pi} \rho(\theta, \omega, k, t) d\theta = 1. \quad (2.38)$$

The continuum equation reads

$$\frac{\partial \rho}{\partial t} = -\frac{\partial}{\partial \theta}(\rho v), \quad (2.39)$$

with

$$v(\theta, \omega, k, t) = \omega + \sigma k \bar{r}(t) \sin(\bar{\psi}(t) - \theta) \quad (2.40)$$

and

$$\bar{r}(t) e^{i\bar{\psi}(t)} = \frac{\int_0^{2\pi} \int_{-\infty}^{\infty} \int_0^{\infty} k e^{i\theta} \rho(\theta, \omega, k, t) g(\omega) P(k) dk d\omega d\theta}{\int_0^{\infty} k P(k) dk}. \quad (2.41)$$

Similarly as in Subsection 2.1.3, one can show that the stationary solutions of (2.39) with constants $\bar{r} > 0$ and $\bar{\psi} = 0$ are

$$\rho(\theta, \omega, k) = \begin{cases} \delta(\theta - \arcsin(\frac{\omega}{\sigma k \bar{r}})), & |\omega| \leq \sigma k \bar{r}, \\ \frac{C(k, \omega)}{|\omega - \sigma k \bar{r} \sin \theta|}, & |\omega| > \sigma k \bar{r}, \end{cases} \quad (2.42)$$

with $C(k, \omega)$ the normalizing factor. By substituting (2.42) into (2.41), one can derive (assuming that g is symmetric) the self-consistency relation

$$\bar{r} e^{i\bar{\psi}} = \frac{\sigma \bar{r} \int_{-\pi/2}^{\pi/2} \int_0^{\infty} \cos^2(\theta) g(\sigma k \bar{r} \sin \theta) k^2 P(k) dk d\theta}{\int_0^{\infty} k P(k) dk}, \quad (2.43)$$

and thus (since $\bar{r} > 0$ and $\bar{\psi} = 0$)

$$1 = \frac{\sigma \int_{-\pi/2}^{\pi/2} \int_0^{\infty} \cos^2(\theta) g(\sigma k \bar{r} \sin \theta) k^2 P(k) dk d\theta}{\int_0^{\infty} k P(k) dk}. \quad (2.44)$$

If we now let $\bar{r} \downarrow 0$ in (2.44), we get the critical coupling:

$$\sigma_c = \frac{2}{\pi g(0)} \frac{\langle k \rangle}{\langle k^2 \rangle} = K_c \frac{\langle k \rangle}{\langle k^2 \rangle}. \quad (2.45)$$

Hence, under the assumption that (2.33) reduces to (2.35), we obtain from (2.45) that the critical coupling σ_c in scale-free networks is just the mean-field critical coupling K_c of (2.20) scaled by the quotient of the first two moments of the degree distribution.

For the distribution given by (2.32), i.e. $P(k) \sim k^{-\gamma}$, one can show that its second moment $\langle k^2 \rangle$ diverges for $\gamma \leq 3$, while it remains finite for $\gamma > 3$. Therefore, according to (2.45), synchronization takes place in scale-free networks with $\gamma \leq 3$ (in particular with $2 < \gamma < 3$, the typical region for real-world networks) as soon as the coupling

strength becomes nonzero. In these ultra small-world networks, the dynamics of the oscillators are driven by the hubs, which lead the population to a state of global synchronization [6].

Furthermore, taking g again to be the standard Gaussian density, the behavior of the order parameter (2.34) near phase transition is investigated in [32]. Assuming the validity of (2.35), it is for this case shown that, in the continuum limit $N \rightarrow \infty$,

$$r \sim (\sigma - \sigma_c)^\beta, \quad \sigma \downarrow \sigma_c \quad (2.46)$$

for scale-free networks with $\gamma > 3$, where the critical exponent takes the value $\beta = 1/2$ if $\gamma \geq 5$, and $\beta = 1/(\gamma - 3)$ if $3 < \gamma \leq 5$. Moreover, for $2 < \gamma < 3$ it is derived in [32] that (2.46) holds with $\beta = 1/(3 - \gamma)$ (and $\sigma_c = 0$ as we have seen above).

Several simulation studies have been performed investigating to what extent the previous analytical results are valid for the model (2.33) [6]. Among these, an interesting result has been found in [50], where scale-free networks with $\gamma = 3$ are considered (constructed with the so-called *Barabási-Albert model*). In this work, simulation results suggest for this case a nonzero critical coupling, which contradicts with the analytical result (2.45). Possible reasons for this inconsistency include in the first place that the assumption of simplifying (2.33) to (2.35) fails as an approximation for this case. Secondly, it could be a finite-size effect, because for $\gamma = 3$ the second moment $\langle k^2 \rangle$ appears to diverge just logarithmically in the Barabási-Albert model as the size of the network size increases [6].

2.3.2.2 Synchronization paths

So far we have considered the onset of global synchronization for the model (2.33). In this subsection we discuss the formation of local synchronization patterns in scale-free networks and, for comparison, in Erdős Rényi networks. To this end, we follow [22, 23] in introducing the local order parameter

$$r_{\text{link}} = \frac{1}{2E} \sum_{i=1}^N \sum_{j \in \mathcal{V}(i)} \left| \lim_{\Delta t \rightarrow \infty} \frac{1}{\Delta t} \int_{t_r}^{t_r + \Delta t} e^{i[\theta_i(t) - \theta_j(t)]} dt \right|, \quad (2.47)$$

where E is the number of edges in the network and t_r is a time sufficiently large for the system to settle into a stationary state. The quantity r_{link} , which lies in the range $[0, 1]$, measures the fraction of pairs of connected nodes in the network that are synchronized (by averaging over a large time interval Δt), and thus provides more information about the existence of synchronized clusters than the modulus r of the order parameter (2.34).

Intriguing results concerning the behavior of r_{link} compared to that of r have been reported in [22] (see also [23]). In this work, paths to synchronization in networks are investigated under the influence of the heterogeneity of the corresponding degree distributions. This has been done by considering scale-free networks (with $\gamma = 3$,

constructed with the Barabási-Albert model) and Erdős-Rényi networks with the same size and average degree. In accordance with the analytical result (2.45), it has been shown with simulations that the critical coupling for the Erdős-Rényi networks is larger than the one for the more heterogeneous scale-free networks, which is depicted in Figure 2.11a. However, as the coupling further increases, the results show that for a certain value of σ the value of r in the Erdős-Rényi case exceeds the one in the scale-free case and remains slightly higher. What we not see from Figure 2.11a is that for both types of networks local synchronization occurs as soon as the coupling strength becomes nonzero, as is shown by the behavior of r_{link} in figure 2.11b. So, interestingly, even when the systems for $\sigma > 0$ are in a state of global incoherence, synchronized components are present in the networks.

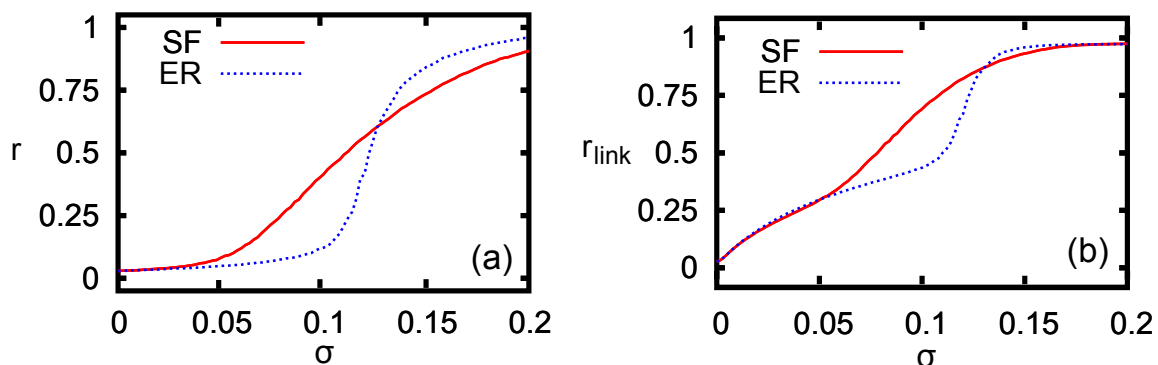


Figure 2.11: Synchronization behavior of the model (2.33) on scale-free (SF) and Erdős-Rényi (ER) networks, based on simulation results of [22]. Shown are the evolution of (a) the global order parameter r of (2.34), and (b) the local order parameter r_{link} of (2.47), both as a function of σ . All results have been obtained with systems relaxed from their initial condition, and with g the uniform frequency distribution on $[-\pi, \pi]$. Furthermore, the networks considered are of size $N = 1000$ with average degree $\langle k \rangle = 6$, where the scale-free networks have degree distribution (2.32) with $\gamma = 3$. Adapted from [22].

To investigate the detailed structure of such synchronized components for both the scale-free and the Erdős-Rényi case, the following symmetric matrix is introduced in [22]:

$$\mathcal{D}_{ij} = a_{ij} \left| \lim_{\Delta t \rightarrow \infty} \frac{1}{\Delta t} \int_{t_r}^{t_r + \Delta t} e^{i[\theta_i(t) - \theta_j(t)]} dt \right|, \quad 1 \leq i, j \leq N, \quad (2.48)$$

where a_{ij} is the adjacency matrix (i.e., $a_{ij} = 1$ if i is connected to j , and 0 otherwise). Fixing a suitable threshold T , for both cases the typical formation of synchronized components — as illustrated in Figure 2.12 — has been obtained by considering oscillators i and j to be synchronized if and only if $\mathcal{D}_{ij} > T$. In the Erdős-Rényi case, small clusters of synchronized nodes are present over the whole network and, when increasing σ through the critical value, spontaneously coalesce to form a single giant component. On the other hand, in the scale-free case the hubs form a central synchronized core and progressively incorporate small components to this core as the coupling increases. This also explains the sharper transition of r_{link} in Figure 2.11b for the Erdős-Rényi case: Whereas in the scale-free networks nodes are absorbed into the core along with

most of their links, what is added in the Erdős-Rényi networks are links connected to nodes already incorporated in the synchronized clusters [2].

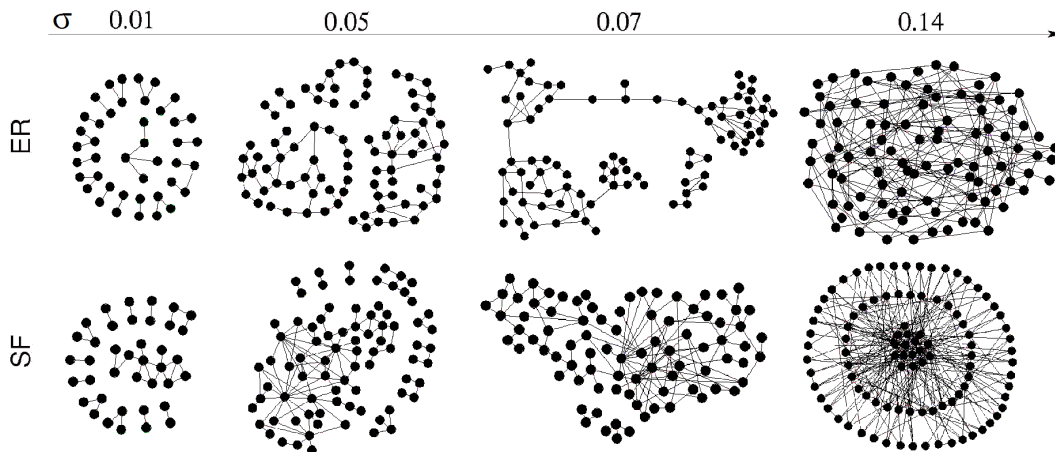


Figure 2.12: Typical evolution of the synchronized components in the scale-free (SF) and the Erdős-Rényi (ER) networks studied in [22], as a function of σ . In the Erdős-Rényi case, small clusters of synchronized oscillators are formed and merge together when the coupling is increased through a certain threshold. In the scale-free case the hubs form a central synchronized core and progressively incorporate small components to this core as the coupling increases. To get a clear picture, the networks used for this figure are of size $N = 100$. Adapted from [22].

2.3.3 Modular networks

In Subsections 2.3.1 and 2.3.2 we considered the synchronization behavior of the Kuramoto model on small-world and scale-free networks, highlighting the effect of the average path length and the degree distribution. However, these topological properties are not sufficient to fully characterize complex networks. In fact, to classify the local connectivity patterns observed in real-world networks with topological quantities could become very difficult. Yet, for several examples such patterns have proved to play an essential role in describing the synchronizability in networks of coupled oscillators. This suggests a reversed approach, namely investigating the Kuramoto model on a network in order to expose the underlying topological structure [6].

A particular example is concerned with modular networks. These are graphs containing a certain number of subgraphs, each of which is internally more connected than with the rest of the graph and thus forms a so-called *community*. Although this informal description of a community might be intuitively clear, it is mathematically not satisfactory. Various precise definitions have been proposed in the literature, but an unambiguous formal description of a community appears to be difficult to establish. Moreover, to find communities algorithmically is a difficult problem, which numerous studies have examined [6]. Interestingly, in [3, 4] a number of networks with ‘well-defined’ communities are considered, for which it is shown that the synchronization behavior of the Kuramoto model is able to successfully detect these communities.

During the process of synchronization, it appears that within each community the oscillators lock their phases on a time scale that depends on the topological structure of the community. To illustrate this, we next consider part of the results obtained in [4], and we refer to [3, 4] for a more comprehensive discussion.

Considered are two different modular networks (described hereafter), each on which the Kuramoto model is defined as

$$\dot{\theta}_i = \sigma \sum_{j \in \mathcal{V}(i)} \sin(\theta_j - \theta_i), \quad i = 1, \dots, N. \quad (2.49)$$

Thus, all oscillators have zero natural frequency, so that the dynamics of the oscillators merely consist in attracting each other (assuming $\sigma > 0$). Therefore, we know that the system eventually settles into a complete synchronized state (i.e., $r = 1$), and it depends on the value of σ and on the topology of the underlying network how long this will take. For a detailed study of the dynamical path to full synchronization, the following time-dependent symmetric matrix is introduced:

$$\rho_{ij}(t) = \langle \cos(\theta_i(t) - \theta_j(t)) \rangle, \quad 1 \leq i, j \leq N, \quad (2.50)$$

where $\langle \dots \rangle$ denotes the average over different initial distributions of the phases. For each pair of oscillators i and j , the local order parameter ρ_{ij} measures its average correlation.

In Figure 2.13, the correlation matrix (2.50) of the two different networks studied in [4] is visualized for the same time instant t . Each of the two networks consists of 256 nodes that are partitioned into four communities of 64 nodes (the second level), each of which is further partitioned into four communities of 16 nodes (the first level). The nodes have an average degree equal to 18. A node in the network corresponding to Figure 2.13 (left), denoted as the 13-4 network, is on average connected to 13 nodes

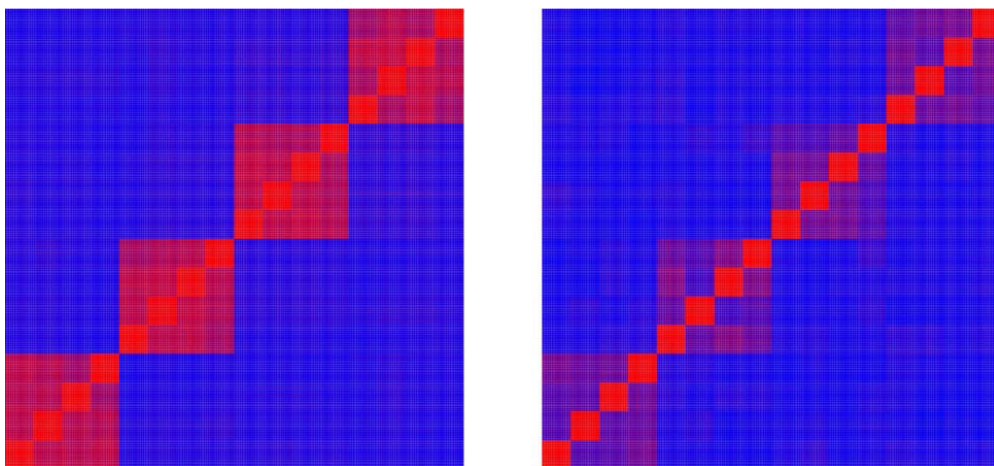


Figure 2.13: Visualization of the correlation matrix (2.50) at a certain time instant t for the 13-4 network (left) and 15-2 network (right) studied in [4]. Colors indicate the correlation, increasing from blue (zero) to red (one).

within the community it is part of at first level, to 4 nodes outside this community but within the community it is part of at second level, and to 1 node elsewhere in the network. A similar structure holds for the 15-2 network corresponding to Figure 2.13 (right). As we see from Figure 2.13, at time t the oscillators within each community at second level in the 13-4 network are almost fully synchronized, whereas those in the 15-2 network are at the start of becoming synchronized. On the other hand, the oscillators in the more densely connected communities at first level are in both cases fully synchronized at time t . This suggests that the communities synchronize in a hierarchical way and on time scales that are smaller for communities internally more connected.

To investigate this quantitatively, the authors of [4] considered the evolution of the dynamical adjacency matrix $\mathcal{D}_T(t)$ given by

$$\mathcal{D}_T(t)_{ij} = \begin{cases} 1, & \rho_{ij}(t) > T, \\ 0, & \rho_{ij}(t) < T, \end{cases} \quad (2.51)$$

where T is a suitable fixed threshold. For each time t the matrix $\mathcal{D}_T(t)$ defines a network in which the connected components are considered to correspond to the synchronized components of the original network. For the studied 13-4 and 15-2 network the obtained results are depicted in Figure 2.14, where the number of disconnected components of \mathcal{D}_T is shown as a function of time. These results clearly show the existence of three time scales, thus revealing the hierarchical structure of the two networks. Moreover, we can observe that full synchronization in the two networks is reached around the same time, but that the stability of the two partitions (indicated by the shadow regions) is different for the two networks.

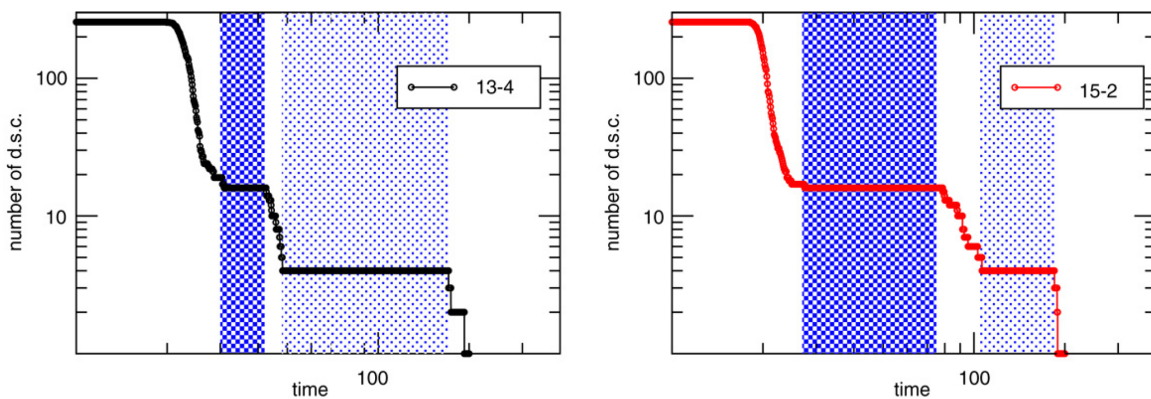


Figure 2.14: Evolution of the number of disconnected synchronized components (d.s.c.) of \mathcal{D}_T (with $T = 0.99$) for the 13-4 network (left) and 15-2 network (right) studied in [4]. The shadow regions mark the stability plateaus for the 16 communities at first level (dark) and the four communities at second level (light). From [2].

Chapter 3

Asymptotic behavior in the noisy mean-field Kuramoto model

3.1 Introduction

In Section 2.1.2 we discussed a continuity equation as a way to describe the mean-field Kuramoto model for the limiting case of infinitely many oscillators. However, a rigorous justification of the validity of this description lacks in the literature. On the other hand, precise convergence results in the limit of a large population have been established for the noisy mean-field Kuramoto model. This model consists of a system of stochastic differential equations, obtained by adding white noise to the governing equations of the mean-field Kuramoto model.

The first purpose of this chapter is to review these convergence results. In particular, we discuss in the next two sections a rigorous treatment for describing the behavior of the noisy model as $N \rightarrow \infty$ with the McKean-Vlasov equation given in (2.26). To this end, we follow parts of Chapters 2 and 3 of the recent PhD thesis of Luçon [34]. It should be mentioned, however, that the first rigorous proof of the convergence of the noisy model to the McKean-Vlasov equation follows from the work by Dai Pra and den Hollander [16], who studied this problem for more general mean-field models using large deviation theory.

With the McKean-Vlasov equation one can prove several synchronization phenomena that are also observed in the mean-field Kuramoto model without noise. Our aim for the second part of this chapter is to give a review of such rigorous results for the noisy model. Specifically, we discuss in Section 3.4 the stationary solutions of the McKean-Vlasov equation, and investigate in Sections 3.5 and 3.6 how these change for different choices of the natural frequency distribution. Since we do not consider any randomness in the population other than the disorder in natural frequencies (and

the white noise), we will from now on simply refer to this randomness as the *disorder* (with this terminology we follow [34]).

In the next section we give a precise description of the noisy mean-field Kuramoto model. For a sufficient understanding of its governing equations — at least in view of the purposes in this thesis — we refer to Section 1 of Appendix A in case the reader is not familiar with stochastic differential equations (SDEs).

3.2 The model

We consider again N oscillators living in the unit circle \mathbb{S} . Their phases $(\theta_i)_{i=1,\dots,N}$ evolve according to the following system of coupled SDEs:

$$d\theta_{i,t} = \omega_i dt + \frac{K}{N} \sum_{j=1}^N \sin(\theta_{j,t} - \theta_{i,t}) dt + 2D dB_{i,t}, \quad i = 1, \dots, N, \quad t \in [0, T], \quad (3.1)$$

in which

- (i) $T > 0$ is a fixed (but arbitrary) time horizon,
- (ii) $K > 0$ is the coupling constant,
- (iii) $(\omega_i)_{i=1,\dots,N}$ are i.i.d. random variables drawn according to some probability law μ on \mathbb{R} (its density with respect to the Lebesgue measure being the previously considered $\omega \mapsto g(\omega)$), referred to as the *law of the disorder*,
- (iv) $(B_i)_{i=1,\dots,N}$ are N i.i.d. standard Brownian motions,
- (v) $D > 0$ is the noise strength.

Furthermore, we let the initial phases be i.i.d. random variables drawn according to some probability law γ on \mathbb{S} , i.e.,

$$(\theta_{i,0})_{i=1,\dots,N} \sim \gamma^N. \quad (3.2)$$

Remark 3.1. In this chapter we will not consider the limiting behavior of the model (3.1) as $D \downarrow 0$ to the mean-field Kuramoto model considered in Section 2.1. For that reason, we set $D := \frac{1}{2}$ from now on for ease of exposition, without loss of generality.

Like in Subsection 2.1.1, by defining the order parameter

$$r_{N,t} e^{i\psi_{N,t}} := \frac{1}{N} \sum_{j=1}^N e^{i\theta_{j,t}}, \quad t \in [0, T], \quad (3.3)$$

we can recast (3.1) into the more convenient form

$$d\theta_i(t) = \omega_i dt + K r_{N,t} \sin(\psi_{N,t} - \theta_{i,t}) dt + dB_{i,t}, \quad i = 1, \dots, N, \quad t \in [0, T]. \quad (3.4)$$

So far, the literature has investigated the behavior of the system defined by (3.2)-(3.4) in the following two ways [34]:

- The *quenched* model: Here, a sequence of random variables $(\omega) := (\omega_i)_{i \in \mathbb{N}}$, i.i.d. according to μ , is drawn once and for all. Then, for each $N \in \mathbb{N}$, the N oscillators have disorder $(\omega_i)_{i=1, \dots, N}$ that is kept fixed during the evolution, so that the behavior of the oscillators is considered under the law of Brownian motion only.
- The *annealed* model: Here, the behavior of the oscillators is considered under the joint law of disorder and Brownian motions. So, as opposed to the quenched model, we average the evolution with respect to the disorder.

For both the quenched and the annealed model the following empirical measure can be successfully used to investigate the behavior of (3.2)-(3.4) as $N \rightarrow \infty$.

Definition 3.2 (Empirical flow). Given oscillators $(\theta_i)_{i=1, \dots, N}$ and disorder $(\omega_i)_{i=1, \dots, N}$, the empirical flow ν_N is defined as

$$\nu_{N,t} := \frac{1}{N} \sum_{j=1}^N \delta_{(\theta_j, t, \omega_j)}, \quad t \in [0, T] \quad (3.5)$$

in which $\delta_{(\theta, \omega)}$ denotes the Dirac measure in $(\theta, \omega) \in \mathbb{S} \times \mathbb{R}$. Thus, ν_N is an element of $\mathcal{C}([0, T], \mathcal{M}_1(\mathbb{S} \times \mathbb{R}))$, where $\mathcal{M}_1(\mathbb{S} \times \mathbb{R})$ denotes the set of probability measures on $\mathbb{S} \times \mathbb{R}$. We use the notation $\nu_N^{(\omega)}$ for the quenched model to specify the dependence of the empirical flow on the fixed sequence (ω) .

The limiting behavior of the random object ν_N as $N \rightarrow \infty$ has been extensively studied in [34], where in a more general setting a law of large numbers is established for ν_N . In both the quenched and annealed model, the empirical flow ν_N appears to converge for $N \rightarrow \infty$ to a deterministic measure ν in $\mathcal{C}([0, T], \mathcal{M}_1(\mathbb{S} \times \mathbb{R}))$ that is the solution of a McKean-Vlasov evolution. It follows from this convergence that the system (3.2)-(3.4) for $N \rightarrow \infty$ can be described by the partial differential McKean-Vlasov equation (2.26), already given in Section 2.1.5. In the following section we will formulate this law of large numbers explicitly, but for the proof (established in a more general setting) we refer to [34].

3.3 McKean-Vlasov equation

In line with [34], we will first consider the *weak formulation* of the McKean-Vlasov equation, of which the solution is the deterministic measure ν around which ν_N will concentrate as $N \rightarrow \infty$. Since the system (3.2)-(3.4) has enough regularity, we will afterwards deduce from this that the density of ν (with respect to the Lebesgue measure) is the strong solution of the system of partial differential equations in (2.26), referred to as the *strong formulation* of the McKean-Vlasov equation.

3.3.1 Weak formulation

We make the following assumption on the law of the disorder μ :

$$\int_{\mathbb{R}} |\omega| d\mu(\omega) < \infty. \quad (3.6)$$

In this case, ν_N satisfies a law of large numbers in the following sense.

Theorem 3.3. *Assume (3.6). Then, in the annealed model, the random variable ν_N converges weakly for $N \rightarrow \infty$ to the unique solution $\nu \in \mathcal{C}([0, T], \mathcal{M}_1(\mathbb{S} \times \mathbb{R}))$ of the weak McKean-Vlasov equation ($t \in [0, T]$)*

$$\begin{aligned} \int_{\mathbb{S} \times \mathbb{R}} \varphi(\theta, \omega) d\nu_t(\theta, \omega) &= \int_{\mathbb{S} \times \mathbb{R}} \varphi(\theta, \omega) d\nu_0(\theta, \omega) \\ &+ \int_0^t \int_{\mathbb{S} \times \mathbb{R}} \frac{\partial \varphi}{\partial \theta}(\theta, \omega) \{ \omega + Kr_s \sin(\psi_s - \theta_s) \} d\nu_s(\theta, \omega) ds \\ &+ \frac{1}{2} \int_0^t \int_{\mathbb{S} \times \mathbb{R}} \frac{\partial^2 \varphi}{\partial \theta^2}(\theta, \omega) d\nu_s(\theta, \omega) ds \end{aligned} \quad (3.7)$$

for every $\varphi \in C_b^2(\mathbb{S} \times \mathbb{R})$ (the set of continuous bounded functions on $\mathbb{S} \times \mathbb{R}$ with two continuous bounded derivatives with respect to the variable $\theta \in \mathbb{S}$), with $\nu_0(d\theta, d\omega) = \gamma(d\theta)\mu(d\omega)$ and

$$r_t e^{i\psi_t} := \int_{\mathbb{S} \times \mathbb{R}} e^{i\theta} d\nu_t(\theta, \omega). \quad (3.8)$$

Moreover, in the quenched model subject to (3.6), the random variable $\nu_N^{(\omega)}$ also converges weakly to ν for $\mu^{\otimes \mathbb{N}}$ -almost every sequence (ω) .

For a precise meaning of this convergence and for the proof, we refer to Theorem 2.16 and Proposition 2.20 of [34]. For a more intuitive understanding, it is instructive to derive the finite-sized equivalent of (3.7) for ν_N and show that the noise must vanish as $N \rightarrow \infty$.

To this end, let $\varphi \in C_b^2(\mathbb{S} \times \mathbb{R})$. By applying Ito's rule in integral form (see Section 2 of Appendix A) as expressed in (A.18) to $f(\theta_{1,t}, \dots, \theta_{N,t}) := \frac{1}{N} \sum_{j=1}^N \varphi(\theta_{j,t}, \omega_j)$, we obtain with the help of (3.4) that

$$\begin{aligned} \frac{1}{N} \sum_{j=1}^N \varphi(\theta_{j,t}, \omega_j) &= \frac{1}{N} \sum_{j=1}^N \varphi(\theta_{j,0}, \omega_j) \\ &+ \int_0^t \frac{1}{N} \sum_{j=1}^N \frac{\partial \varphi}{\partial \theta}(\theta_{j,s}, \omega_j) \{ \omega_j + Kr_{N,s} \sin(\psi_{N,s} - \theta_{j,s}) \} \\ &+ \frac{1}{2} \int_0^t \frac{1}{N} \sum_{j=1}^N \frac{\partial^2 \varphi}{\partial \theta^2}(\theta_{j,s}, \omega_j) + \int_0^t \frac{1}{N} \sum_{j=1}^N \frac{\partial \varphi}{\partial \theta}(\theta_{j,s}, \omega_j) dB_{j,s}. \end{aligned} \quad (3.9)$$

Now, from the definition of $\nu_{N,t}$ in (3.5), it follows that

$$\begin{aligned} \int_{\mathbb{S} \times \mathbb{R}} \varphi(\theta, \omega) d\nu_{N,t}(\theta, \omega) &= \int_{\mathbb{S} \times \mathbb{R}} \varphi(\theta, \omega) d\nu_{N,0}(\theta, \omega) \\ &\quad + \int_0^t \int_{\mathbb{S} \times \mathbb{R}} \frac{\partial \varphi}{\partial \theta}(\theta, \omega) \{\omega + Kr_{N,s} \sin(\psi_{N,s} - \theta)\} d\nu_{N,s}(\theta, \omega) ds \\ &\quad + \frac{1}{2} \int_0^t \int_{\mathbb{S} \times \mathbb{R}} \frac{\partial^2 \varphi}{\partial \theta^2}(\theta, \omega) d\nu_{N,s}(\theta, \omega) ds + M_{N,t}(\varphi) \end{aligned} \quad (3.10)$$

(compare with (3.7)), where we defined

$$M_{N,t}(\varphi) := \frac{1}{N} \sum_{j=1}^N \int_0^t \frac{\partial \varphi}{\partial \theta}(\theta_{j,s}, \omega_j) dB_{j,s}. \quad (3.11)$$

Similarly as in [7], one can show

$$\mathbb{E} \left[\sup_{t \in [0, T]} (M_{N,t}(\varphi))^2 \right] \leq \frac{T}{N} \left\| \frac{\partial \varphi}{\partial \theta} \right\|_{\infty}^2, \quad (3.12)$$

which indeed ensures that the noise in (3.10) vanishes as $N \rightarrow \infty$ and therefore confirms that the limit ν is not random. (Note, however, that this does not prove its uniqueness nor its existence.)

3.3.2 Strong formulation

The following proposition is a special case of Proposition 3.1 in [34], to which we refer the reader for a proof.

Proposition 3.4. *Consider the unique solution $\nu \in \mathcal{C}([0, T], \mathcal{M}_1(\mathbb{S} \times \mathbb{R}))$ to (3.7) with $\nu_0(d\theta, d\omega) = \gamma(d\theta)\mu(d\omega)$. Then, for all $t \in (0, T]$, ν_t is absolutely continuous with respect to $\lambda \otimes \mu$ (with λ denoting the Lebesgue measure on \mathbb{S}) and, for μ -almost every $\omega \in \text{supp}(\mu)$, the corresponding density $(t, \theta, \omega) \mapsto p_t(\theta, \omega)$ is strictly positive on $(0, T] \times \mathbb{S}$, is \mathcal{C}^∞ in t and θ , and solves the (strong) McKean-Vlasov equation*

$$\frac{\partial p_t(\theta, \omega)}{\partial t} = -\frac{\partial}{\partial \theta} (p_t(\theta, \omega) \{\omega + Kr_t \sin(\psi_t - \theta)\}) + \frac{1}{2} \frac{\partial^2 p_t(\theta, \omega)}{\partial \theta^2}, \quad (3.13)$$

where

$$r_t e^{i\psi_t} = \int_{\mathbb{R}} \int_0^{2\pi} e^{i\theta} p_t(\theta, \omega) d\theta d\mu(\omega). \quad (3.14)$$

The following remarks are in order:

Remark 3.5. We can retrieve the weak formulation in (3.7) by multiplying (3.13) with $\varphi \in C_b^2(\mathbb{S} \times \mathbb{R})$, integrating over $\mathbb{S} \times \mathbb{R}$ and using integration by parts. What makes the formulation of the McKean-Vlasov equation in (3.13) stronger than in (3.7), is that a solution $(t, \theta, \omega) \mapsto p_t(\theta, \omega)$ of (3.13) is required to be differentiable w.r.t. t

and θ (at least twice w.r.t. θ), whereas a solution $(t, \theta, \omega) \mapsto p_t(\theta, \omega)$ of (3.7) with $\nu_t(d\theta, d\omega) = p_t(\theta, \omega)d\theta\mu(d\omega)$ is a priori not necessarily differentiable w.r.t. t and θ .

Remark 3.6. Just as we remarked for (2.9), it is important to note that the number of (coupled) equations that the McKean-Vlasov equation represents depends on the cardinality of $\text{supp}(\mu)$, which is the support of μ . Moreover, the density $\theta \mapsto p_t(\theta, \omega)$ is 2π -periodic seen as a function of θ in \mathbb{R} and can be taken to be normalized, as is the case for ρ in (2.7) and (2.8), respectively. On the other hand, ρ does not satisfy the smooth properties of p in Proposition 3.4.

From Theorem 3.3 and Proposition 3.4 follows that the McKean-Vlasov equation (3.13) describes the behavior of the model on the scale of the law of large numbers. For the quenched model, a central limit theorem associated to this convergence has been established in [33] (which is also included in [34]), where it is shown that the fluctuation process

$$\eta_N^{(\omega)} := \sqrt{N}(\nu_N^{(\omega)} - \nu) \quad (3.15)$$

converges in a weak sense as $N \rightarrow \infty$ (see Theorem 2.10 in [33] for details). From this fluctuation theorem, a similar central limit theorem for the averaged model is derived in [34].¹ Moreover, the quenched fluctuation process $\mathcal{R}_N^{(\omega)}$ defined by

$$\mathcal{R}_{N,t}^{(\omega)} := \sqrt{N}(r_{N,t}^{(\omega)} - r_t), \quad t \in [0, T] \quad (3.16)$$

also converges in a weak sense as $N \rightarrow \infty$ (see Theorem 2.13 in [33]), which might be comparable with the scaling $N^{-1/2}$ for the fluctuations of the order parameter (2.3) discussed in Subsection 2.1.5 for the mean-field Kuramoto model without noise. Other rigorous fluctuation results are for instance found in [12], where the dynamics of (3.1) with $N \rightarrow \infty$ are considered for the case that the coupling is close to its critical value.

3.4 Stationary solutions of the McKean-Vlasov equation

In the previous section we focused on the behavior of the noisy mean-field Kuramoto model as $N \rightarrow \infty$ on a *finite* time interval. On the scale of the law of large numbers, the McKean-Vlasov equation (3.13) is in this case the relevant object to study. We will now consider this system in the limit $t \rightarrow \infty$. Considering our study of the mean-field Kuramoto model in Section 2.1, a good starting point for this is to determine the stationary solutions of the McKean-Vlasov equation in the frame rotating with the average phase. In this frame the mean of μ is zero, i.e.,

$$\int_{\mathbb{R}} \omega d\mu(\omega) = 0, \quad (3.17)$$

¹Both the quenched and averaged central limit theorem are derived in [33, 34] for more general models than Kuramoto's model. For part of these models for which the interaction is governed by an Hamiltonian (this includes Kuramoto's model), this averaged central limit theorem has been first established in [16], where a different empirical measure (the so-called *double-layer empirical measure*) is used.

without loss of generality (recall (2.2)).

From now on we assume (3.17) and proceed as in [34] (see also [25, 40]). A stationary solution $p(\theta, \omega)$ of (3.13) satisfies

$$0 = -\frac{\partial}{\partial \theta} (p(\theta, \omega) \{\omega + Kr \sin(\psi - \theta)\}) + \frac{1}{2} \frac{\partial^2 p(\theta, \omega)}{\partial \theta^2}, \quad (3.18)$$

where the constants r and ψ must be consistent with

$$re^{i\psi} = \int_{\mathbb{R}} \int_0^{2\pi} e^{i\theta} p(\theta, \omega) d\theta d\mu(\omega). \quad (3.19)$$

Note that by rotation symmetry we can assume $\psi = 0$ without loss of generality, so that (3.18) reduces to

$$0 = -\frac{\partial}{\partial \theta} (p(\theta, \omega) \{\omega - Kr \sin(\theta)\}) + \frac{1}{2} \frac{\partial^2 p(\theta, \omega)}{\partial \theta^2}. \quad (3.20)$$

Integrating this equation twice w.r.t. θ introduces two constants (depending on ω), which can be determined from the normalization and periodicity condition on $p(\theta, \omega)$. In doing so, we arrive at solutions of the form

$$p(\theta, \omega, r) = \frac{1}{Z(\omega, r)} A(\theta, \omega, r), \quad (3.21)$$

with

$$A(\theta, \omega, r) = B(\theta, \omega, r) \left\{ e^{4\pi\omega} \int_0^{2\pi} \frac{dx}{B(x, \omega, r)} + (1 - e^{4\pi\omega}) \int_0^\theta \frac{dx}{B(x, \omega, r)} \right\}, \quad (3.22)$$

$$B(\theta, \omega, r) = \exp(2Kr \cos \theta + 2\omega\theta), \quad (3.23)$$

for $\theta \in [0, 2\pi)$ and $\omega \in \text{supp}(\mu)$, with normalizing constant

$$Z(\omega, r) = \int_0^{2\pi} A(\theta, \omega, r) d\theta, \quad \omega \in \text{supp}(\mu). \quad (3.24)$$

Hence, from (3.19) with $\psi = 0$ it follows that $p(\theta, \omega, r)$ given by (3.21)-(3.24) is a stationary solution of (3.13) if and only if r satisfies

$$\begin{cases} r = \int_{\mathbb{R}} \int_0^{2\pi} \cos(\theta) p(\theta, \omega, r) d\theta d\mu(\omega), \\ 0 = \int_{\mathbb{R}} \int_0^{2\pi} \sin(\theta) p(\theta, \omega, r) d\theta d\mu(\omega). \end{cases} \quad (3.25)$$

Now, note that for any choice of μ and K , the incoherent solution from Subsection 2.1.2,

$$p(\theta, \omega) = \frac{1}{2\pi}, \quad r = 0, \quad (3.26)$$

satisfies (3.21)-(3.25) and is the only stationary solution with $r = 0$. To find synchronized solutions (i.e., solutions with $r > 0$) is in general very complicated, but matters improve considerably when μ is symmetric. In that case, due to the symmetry

$p(\theta, \omega, r) = p(-\theta, -\omega, r)$ possessed by (3.21), the second equation in (3.25) is always satisfied. Hence, by defining

$$\Phi_\mu(r) := \int_{\mathbb{R}} \frac{\int_0^{2\pi} \cos(\theta) A(\theta, \omega, r) d\theta}{Z(\omega, r)} d\mu(\omega), \quad (3.27)$$

the problem then comes down to investigating the solutions of the *consistency relation*

$$r = \Phi_\mu(r). \quad (3.28)$$

We will treat the symmetric case in Section 3.5. Before that, however, it is illuminating to consider the case when there is no disorder, i.e., $\mu = \delta_0$. Then the model exhibits a phase transition that is well understood.

3.5 Limiting dynamics in the case of no disorder

With $\mu = \delta_0$ the McKean-Vlasov equation (3.13) reduces to the single partial differential equation

$$\frac{\partial p_t(\theta)}{\partial t} = -\frac{\partial}{\partial \theta} (p_t(\theta) K r_t \sin(\psi_t - \theta_t)) + \frac{1}{2} \frac{\partial^2 p_t(\theta)}{\partial \theta^2}, \quad (3.29)$$

where

$$r_t e^{i\psi_t} = \int_0^{2\pi} e^{i\theta} p_t(\theta) d\theta. \quad (3.30)$$

Using the results of the previous section, one is able to prove the following:

Proposition 3.7 (See Proposition 3.8 in [34]). *Define $K_c := 1$.*

- (a) *For $K \leq K_c$, the incoherent solution (3.26) is the only stationary solution of (3.29).*
- (b) *For $K > K_c$, the stationary solutions of (3.29) consist of the incoherent solution (3.26) and a unique synchronized solution (in fact, by rotation invariance, a unique circle of synchronized solutions).*

Proof. It follows from (3.21)-(3.24) with $\omega = 0$ that the stationary solutions of (3.29) are of the form

$$p(\theta, r) = \frac{1}{Z(r)} e^{2Kr \cos(\theta)}, \quad \theta \in [0, 2\pi), \quad (3.31)$$

with $Z(r) = \int_0^{2\pi} e^{2Kr \cos(\theta)} d\theta$. Here, r satisfies the consistency relation $r = \Phi_\mu(r)$, with

$$\Phi_\mu(r) = \frac{\int_0^{2\pi} \cos(\theta) e^{2Kr \cos(\theta)} d\theta}{Z(r)}. \quad (3.32)$$

It is not difficult to verify that the map $r \mapsto \Phi_\mu(r)$ is continuous and strictly concave, with $\Phi_\mu(0) = 0$, $\Phi'_\mu(0) = K$ and $\lim_{r \rightarrow \infty} \Phi_\mu(r) = 1$. Therefore, when $K > K_c$, the

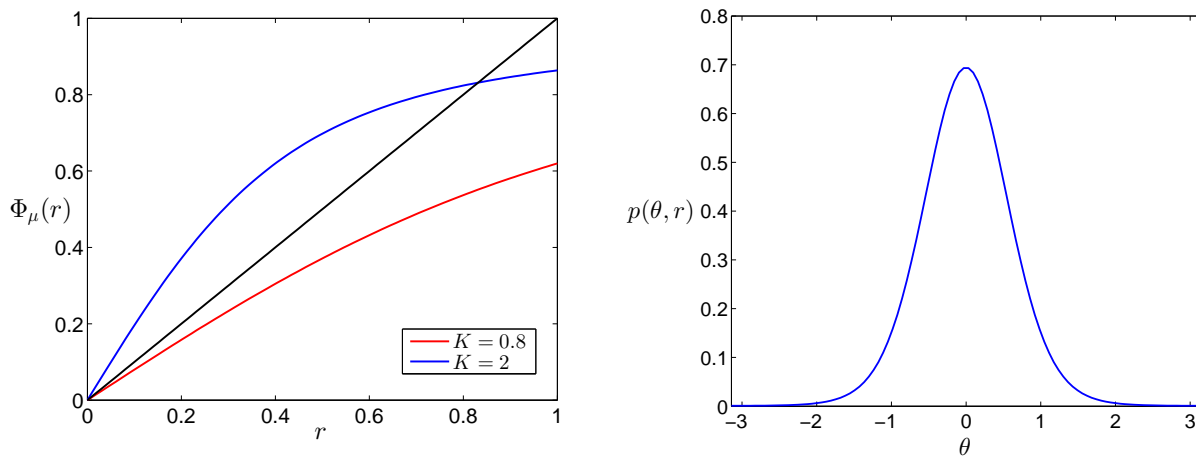


Figure 3.1: Left: Plot of $r \mapsto \Phi_\mu(r)$ with $\mu = \delta_0$ for two choices of K . For $K \leq 1$ (red), $r = 0$ is the only solution of $r = \Phi_\mu(r)$, while for $K > 1$ (blue), there is a unique synchronized solution $r > 0$ to $r = \Phi_\mu(r)$. Right: Plot of the synchronized solution (3.31) for $K = 2$.

slope of $r \mapsto \Phi_\mu(r)$ exceeds 1, which must yield a solution $r > 0$ of $r = \Phi_\mu(r)$ to satisfy the limit $\lim_{r \rightarrow \infty} \Phi_\mu(r) = 1$ (see Figure 3.1). Due to the strict concavity of $r \mapsto \Phi_\mu(r)$, we know that this synchronized solution is unique for $K > K_c$, and that $r = 0$ is the only solution of $r = \Phi_\mu(r)$ for $K \leq K_c$. \square

In [21] it is rigorously shown that for $K \leq K_c$ the incoherent solution is the the global attractor of the system (3.29), whereas for $K > K_c$ this solution becomes unstable and the synchronized solutions become asymptotically stable. Hence, when K is increased through K_c , the system undergoes a phase transition from the incoherent state to a synchronized state.

3.6 Limiting dynamics in the case of symmetric disorder

Just as for the special case of no disorder, we have seen in Section 3.4 that for symmetric μ there is a one-to-one correspondence between the stationary solutions of (3.13) and the solutions $r \in [0, 1]$ of the consistency relation $r = \Phi_\mu(r)$, of which the right-hand side is given in (3.27). The main difference with the non-disordered case, however, is that for symmetric disorder the map $r \mapsto \Phi_\mu(r)$ is not concave in general. As a result, several problems concerning existence and uniqueness of synchronized solutions are still open. For general symmetric disorder, we can at least say the following [34]:

Proposition 3.8. *Suppose that μ is symmetric. Define*

$$\tilde{K} := \left(\int_{\mathbb{R}} \frac{d\mu(\omega)}{1 + 4\omega^2} \right)^{-1}. \quad (3.33)$$

- (a) The incoherent solution (3.26) is the only stationary solution of (3.13) provided that K does not exceed a certain threshold K_c , which is bounded by \tilde{K} .
- (b) For $K > \tilde{K}$, the stationary solutions of (3.13) consist of the incoherent solution (3.26) and at least one synchronized solution (in fact, by rotation invariance, at least one circle of synchronized solutions).

Proof. Again, straightforward calculations show that the map $r \mapsto \Phi_\mu(r)$ is continuous such that $\Phi_\mu(0) = 0$, $\Phi'_\mu(0) = K/\tilde{K}$ and $\lim_{r \rightarrow \infty} \Phi_\mu(r) = 1$ (see [25] for details). From what we have seen in the proof of Proposition 3.7, this is enough to yield the desired result. \square

We now turn our attention to two special cases of symmetric disorder that have been frequently investigated in the literature, the first one being the case that μ is furthermore assumed to be unimodal.

3.6.1 Unimodal disorder

It is believed that for μ symmetric and unimodal the map $r \mapsto \Phi_\mu(r)$ is strictly concave [34]. If true, then Proposition 3.7 would also apply to this case, but with K_c equal to \tilde{K} . Furthermore, for the synchronized solution of which we know by proposition 3.8(b) to appear when $K > \tilde{K}$, one can use a Taylor expansion to show that it bifurcates supercritically from the incoherent solution as $r \sim C\sqrt{K - \tilde{K}}$, $K \downarrow \tilde{K}$ (with $C > 0$) when μ is unimodal and symmetric (see [25] for details). Moreover, in [47] it is shown that in this case the incoherent solution is linearly stable for $K < \tilde{K}$ and unstable for $K > \tilde{K}$.

Thus, it seems likely that in this case a phase transition occurs from the incoherent solution to a synchronized solution when K exceeds \tilde{K} , similar to what we discussed in Section 2.1.3.

Remark 3.9. Recall that we have set $D = \frac{1}{2}$ in (3.1) (see Remark 3.1). For general $D > 0$, we would have found that \tilde{K} should be defined as

$$\tilde{K} := 2 \left(\int_{\mathbb{R}} \frac{D}{D^2 + \omega^2} d\mu(\omega) \right)^{-1} \quad (3.34)$$

to satisfy proposition 3.8. As $D \downarrow 0$, this equation reduces to Kuramoto's critical coupling (2.20) for the mean-field Kuramoto model with μ symmetric and unimodal [42].

As an illustration, we consider the case that the law of disorder is Lorentzian, meaning that the density of μ with respect to the Lebesgue measure is given by (2.22). The expression in (3.33) then reduces to $\tilde{K} = 2\Delta + 1$, and simulation results like those in Figure 3.2 suggest that $K_c = \tilde{K}$. Moreover, the bifurcation of the partially synchronized state from the incoherent state is in this case well approximated by (2.23).

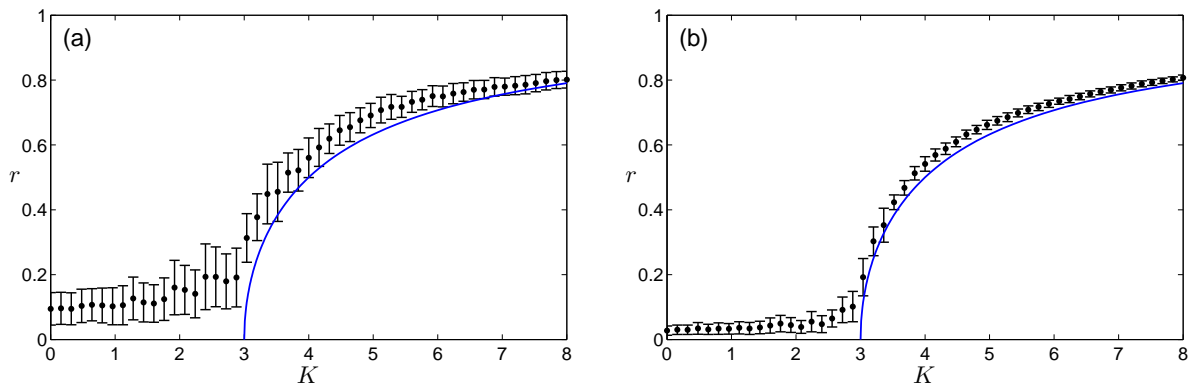


Figure 3.2: Phase diagram for the model (3.1) with $D = 1/2$ and in the case of the Lorentzian frequency distribution (2.22) with $\Delta = 1$. Figures (a) and (b) show the simulation results obtained with $N = 100$ and $N = 1000$ oscillators, respectively, having natural frequencies that are the same for each evaluated K . In both figures, (2.23) with $K_c = 3$ is plotted in blue for comparison. For each investigated K , the corresponding r is the result from averaging over a time period after the system has settled into a stationary state, with error bars representing standard deviations. As numerical integration scheme the Milstein algorithm (see Appendix A) is used, and the corresponding Matlab code is provided in Section 2 of Appendix B.

Thus, for a Lorentzian frequency distribution, the phase diagram of the mean-field Kuramoto model (Figure 3.2) with noise closely resembles the one without noise (Figure 2.3). Indeed, the noise just introduces more randomness into the model, so that the critical coupling for phase transition is larger.

3.6.2 Binary disorder

We next discuss the example in which the disorder takes the form $\mu = \frac{1}{2}(\delta_{-\omega_0} + \delta_{\omega_0})$, with $\omega_0 > 0$. For suitable choices of K and ω_0 , concavity of Φ_μ fails, so that in these cases the phase transition is not merely determined by the slope of Φ_μ at the origin.

To see why, we follow [34] in investigating the behavior of $r \mapsto \Phi_\mu(r)$ around the origin by fixing some $K > 1$ and letting ω_0 run from 0 to ∞ . We have the following:

- With Proposition 3.8 we find $\Phi'_\mu(0) = \frac{K}{1+4\omega_0^2}$. By defining $\omega_s(K) := \frac{\sqrt{K-1}}{2}$, we therefore see that the slope of Φ_μ at the origin is larger than 1 if and only if $\omega \leq \omega_s(K)$.
- By direct calculations (see [25] for details) it follows that $\Phi''_\mu(0) = 0$ and $\Phi'''_\mu(0) = -6K^3D(\omega_0)$ with

$$D(\omega_0) := \frac{1}{2(1+\omega_0^2)} - \frac{8\omega_0^2}{(1+4\omega_0^2)^2}. \quad (3.35)$$

Defining $\omega_c := \frac{1}{2\sqrt{2}}$, it is not difficult to verify that $D(\omega_0) > 0$ for $0 \leq \omega_0 < \omega_c$, whereas $D(\omega_0) < 0$ for $\omega_0 > \omega_c$. Therefore, near the origin, the map $r \mapsto \Phi_\mu(r)$ is locally concave for $0 \leq \omega_0 < \omega_c$ and locally convex for $\omega_0 > \omega_c$.

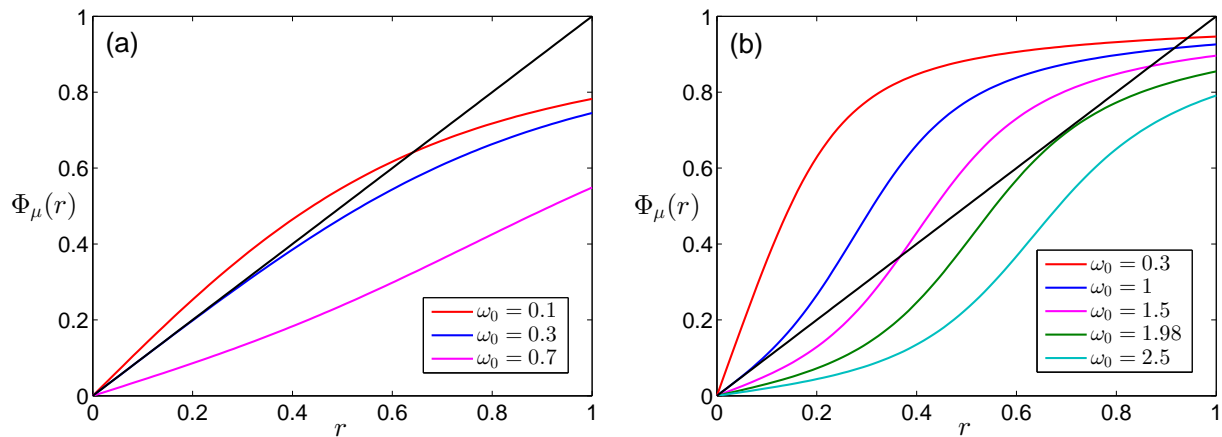


Figure 3.3: Plot of $r \mapsto \Phi_\mu(r)$ with $\mu = \frac{1}{2}(\delta_{-\omega_0} + \delta_{\omega_0})$ for two choices of K and several choices of ω_0 . (a) The regime $1 < K \leq \frac{3}{2}$ is illustrated with $K = 1.36$. In this case, $\omega_s(K) = 0.3$ is smaller than $\omega_c = \frac{1}{2\sqrt{2}} \approx 0.35$, so that Φ_μ is convex near the origin if and only if $\Phi'_\mu(0) \leq \frac{K}{1+4\omega_c^2} \approx 0.91$. (b) The regime $K > \frac{3}{2}$ is illustrated with $K = 5$. In this case, $\omega_s(K) = 1$ is larger than $\omega_c \approx 0.35$, so that Φ_μ is convex near the origin if and only if $\Phi'_\mu(0) \leq \frac{K}{1+4\omega_c^2} \approx 3.33$.

Solving $\omega_s(K) = \omega_c$ for K we get $K = \frac{3}{2}$. Therefore we distinguish between the regimes $1 < K \leq \frac{3}{2}$ and $K > \frac{3}{2}$. As we let ω_0 run from 0 to ∞ , we find that in the regime $1 < K \leq \frac{3}{2}$ (which corresponds to $\omega_s(K) \leq \omega_c$) the change of the slope of Φ_μ through the critical value 1 happens before the change of local concavity (see Figure 3.3a), whereas the reversed order occurs for $K > \frac{3}{2}$ (see Figure 3.3b). In particular, the latter case shows that a synchronized solution can exist even when the slope of Φ_μ at the origin is smaller than 1, and that two distinct synchronized solutions can coexist. (The one with the smallest value of r is typically unstable.)

The phase diagram in the case of binary disorder has been obtained (partly numerically) in [15] (see also [9]) and shows many similarities with that of the bimodal case in Figure 2.5. Also in this case the phase diagram includes regions of incoherence, partial synchronization, standing waves and bistability, which are similar in shape when the noise strength D is identified with the width parameter Δ in Figure 2.5. Indeed, as it is formulated in [35], “the noise blurs the δ -functions into bell-shaped distributions analogous to Lorentzians or Gaussians.” In the case of Figure 3.3b, for instance, the coupling is strong enough such that for increasing ω_0 the system undergoes a transition from partially synchronized to a state of standing waves.

Chapter 4

A Kuramoto-like model on the hierarchical lattice

4.1 Introduction

For the noisy mean-field Kuramoto model, significant rigorous results are obtained in the mathematical literature, of which we have discussed a considerable part in Chapter 3. On the other hand, the mathematical literature barely contains rigorous results for the Kuramoto model on general networks, which, as we have seen in Chapter 2, covers a rich phenomenology. We discuss in this chapter a rigorous treatment for a Kuramoto-like model on the hierarchical lattice, which deals with more general interactions than the noisy mean-field Kuramoto model.

A precise description of the model we consider is given in (4.5) in Section 4.3, where its governing equations are defined as a system of SDEs on the hierarchical lattice. For this, we first consider in Section 4.2 the so-called hierarchical group of order N , which mathematically characterizes this hierarchical lattice. At each hierarchical level $k \in \mathbb{N}_0$, the population can then be thought of as partitioned into so-called k -blocks of N^k oscillators, so that each oscillator is coupled with a strength $O(N^{-2k-1})$ to the oscillators outside the k -block it is part of. Moreover, in the model, natural frequencies are not only assigned to each oscillator, but also to each block of oscillators. Roughly speaking, synchronization in the model is then passed from 1-blocks to 2-blocks and so on, each transmission following more or less the evolution of a noisy Kuramoto model at a time scale proportional to the size of the blocks.

We are interested in the behavior of the model in (4.5) in the so-called hierarchical mean-field limit $N \rightarrow \infty$. In several studies (see [26] and references therein), systems of hierarchically interacting diffusions are considered that allow for a rigorous renormalization analysis in this hierarchical mean-field limit. The components in a k -block then reach a state of equilibrium on time scale $N^k t$, so that the limit $N \rightarrow \infty$ yields a

separation of successive space-time scales [26]. However, in these studied systems the components in the blocks are *linearly* attracted, whereas in the model we consider the components (i.e., the oscillators) are sinusoidally and thus *nonlinearly* coupled. Hence, it requires a more complex renormalization program compared to the one carried out in [26] to obtain rigorous results on the synchronization behavior of (4.5) in the limit $N \rightarrow \infty$. In Section 4.4 we outline a preliminary analysis for such a program, where we provide some exact results in Subsection 4.4.1 and discuss the behavior we expect from (4.5) for $N \rightarrow \infty$ in Subsection 4.4.2.

4.2 The hierarchical group of order N

The *hierarchical group* Ω_N of order $N \in \mathbb{N} \setminus \{1\}$ is the set

$$\Omega_N = \left\{ \eta = (\eta^l)_{l \in \mathbb{N}_0} \in \{0, 1, \dots, N-1\}^{\mathbb{N}_0} : \sum_{l \in \mathbb{N}_0} \eta^l < \infty \right\}, \quad (4.1)$$

equipped with addition modulo N , i.e., $(\eta + \zeta)^l := \eta^l + \zeta^l \pmod{N}$, $l \in \mathbb{N}_0$. A visual interpretation of Ω_N is given in Figure 4.1, where the elements of Ω_N can be identified with the leaves of the tree. On Ω_N , the *ultrametric distance* is defined as

$$d : \Omega_N \times \Omega_N \rightarrow \mathbb{N}_0, \quad (\eta, \zeta) \mapsto \min\{k \in \mathbb{N}_0 : \eta^l = \zeta^l \forall l \geq k\}. \quad (4.2)$$

For $\eta \in \Omega_N$ and $k \in \mathbb{N}_0$, let $B_k(\eta)$ denote the k -block around η , given by

$$B_k(\eta) := \{\zeta \in \Omega_N : d(\eta, \zeta) \leq k\}. \quad (4.3)$$

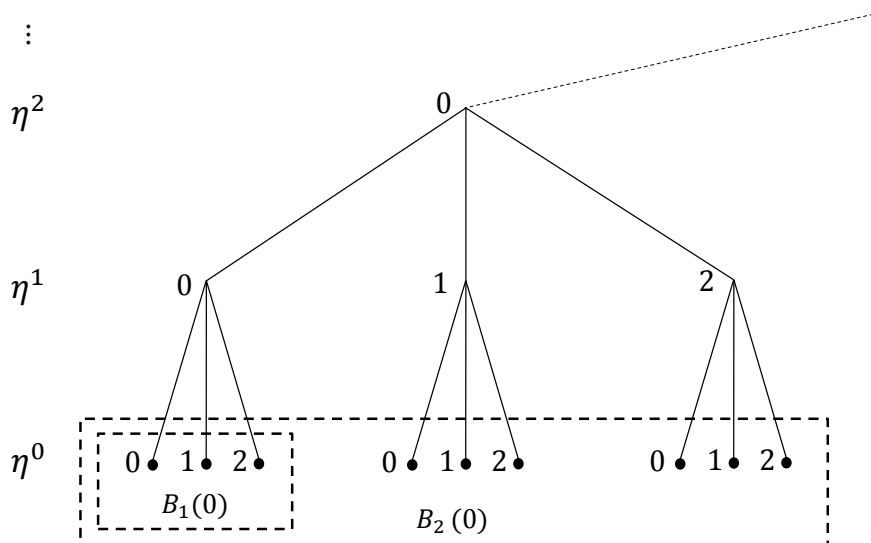


Figure 4.1: Geometry of Ω_N for $N = 3$. A sequence $(\eta^l)_{l \in \mathbb{N}_0} \in \Omega_N$ is visualized as a path of numbers and can be identified with its corresponding leaf in the tree. Furthermore, the blocks $B_1(0)$ and $B_2(0)$ around the origin $(0, 0, \dots) \in \Omega_N$ are pictured, which contain the elements of Ω_N up to (ultrametric) distance 1 and 2 from the origin, respectively.

For the model (4.5) we consider in Section 4.3, we can think of the oscillators as the leaves of the tree. Moreover, each distance $i \in \mathbb{N}$ is ascribed a coupling constant $K_i > 0$, so that each pair of oscillators $\eta, \zeta \in \Omega_N$ with $d(\eta, \zeta) = i$ tend to attract each other with strength K_i/N^{2i-1} . In order to assign to each block a natural frequency, however, we need to consider all the nodes of the tree instead of only its leaves.

To this end, we follow [24] in defining the *full tree* as

$$\Omega_N^{\mathbb{T}} = \bigcup_{k \in \mathbb{N}_0} \Omega_N^{(k)}, \quad \text{with} \quad \Omega_N^{(k)} = \Omega_N/B_k(0). \quad (4.4)$$

In (4.4), $\Omega_N/B_k(0)$ denotes the quotient group of Ω_N modulo $B_k(0)$, and its elements can be identified with the nodes in the tree at hierarchical level k (see Figure 4.2). Furthermore, for $\eta \in \Omega_N$ and $k \in \mathbb{N}_0$, we denote $[\eta]_k$ for the equivalence class in $\Omega_N^{(k)}$ of which η is an element.

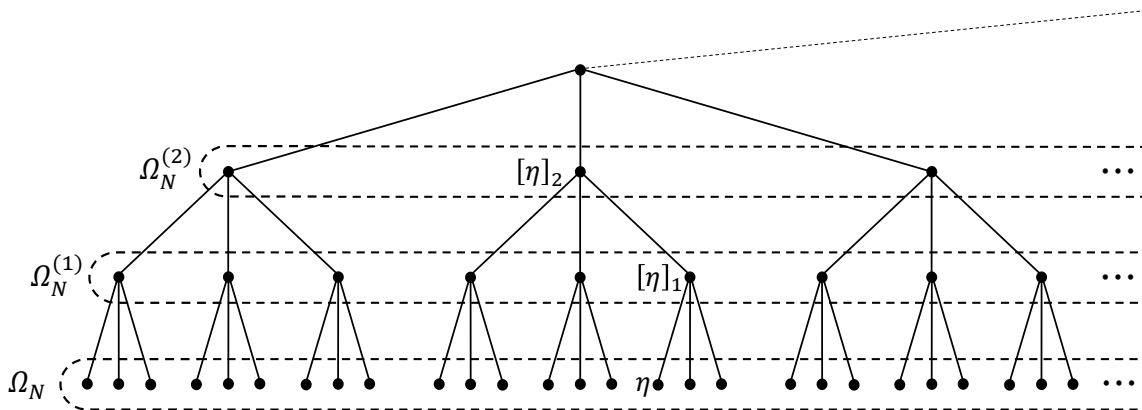


Figure 4.2: Visual interpretation of $\Omega_N^{\mathbb{T}}$ for $N = 3$. The elements of $\Omega_N^{\mathbb{T}}$ can be identified with the nodes in the tree, which are partitioned into sets of nodes $\Omega_N^{(k)}$ at distinct hierarchical levels $k \in \mathbb{N}_0$. As shown, an equivalence class $[\eta]_k$ of $\eta \in \Omega_N$ then corresponds to the ancestor at hierarchical level k of the associated node. Adapted from [24].

4.3 The model

We consider oscillators $(\theta_\eta)_{\eta \in \Omega_N}$ living in the unit circle \mathbb{S} and evolving according to the following system of coupled SDEs:

$$d\theta_{\eta,t} = \sum_{i \in \mathbb{N}_0} N^{-i} \omega_{[\eta]_i} dt + \sum_{\zeta \in \Omega_N} \frac{K_{d(\zeta, \eta)}}{N^{2d(\zeta, \eta)-1}} \sin(\theta_{\zeta,t} - \theta_{\eta,t}) dt + dB_{\eta,t}, \quad \eta \in \Omega_N, t \geq 0, \quad (4.5)$$

in which

- (i) $(K_i)_{i \in \mathbb{N}} \in (0, \infty)^{\mathbb{N}}$ are the coupling constants,
- (ii) for each $i \in \mathbb{N}_0$, $(\omega_\xi)_{\xi \in \Omega_N^{(i)}}$ are i.i.d. random variables drawn according to some probability law μ_i on \mathbb{R} , referred to as the *law of disorder on scale i* ,
- (iii) $(B_\eta)_{\eta \in \Omega_N}$ are i.i.d. standard Brownian motions.

Furthermore, we let the initial phases be i.i.d. random variables drawn according to some probability law γ on \mathbb{S} , i.e.,

$$\theta_{\eta,0} \sim \gamma, \quad \eta \in \Omega_N. \quad (4.6)$$

To investigate the synchronization behavior of the system given by (4.5) and (4.6), we define for each k -block an order parameter as

$$R_{\eta,Nt}^{[k]} e^{i\Phi_{\eta,t}^{[k]}} := \frac{1}{N^k} \sum_{\zeta \in B_k(\eta)} e^{i\theta_{\zeta,N^k t}}, \quad \eta \in \Omega_N, t \geq 0, \quad (4.7)$$

so that the average phase in the k -block is measured by $\Phi_{\eta,t}^{[k]}$, which is called a *block average on space-time scale k* , and $R_{\eta,Nt}^{[k]}$ measures the phase coherence in the block. The chosen time scales in (4.7) will be motivated below. With (4.7) and the observation that for each $\eta \in \Omega_N$ we have

$$\sum_{\zeta \in \Omega_N} \frac{K_{d(\zeta,\eta)}}{N^{2d(\zeta,\eta)}} \sin(\theta_{\zeta,t} - \theta_{\eta,t}) = \sum_{i \in \mathbb{N}} \frac{K_i}{N^{2i}} \sum_{\zeta \in B_i(\eta)/B_{i-1}(\eta)} \sin(\theta_{\zeta,t} - \theta_{\eta,t}), \quad (4.8)$$

we can write (4.5) into the form

$$d\theta_{\eta,t} = \sum_{i \in \mathbb{N}_0} N^{-i} \omega_{\eta}^{[i]} dt + \sum_{i \in \mathbb{N}} \frac{1}{N^{i-1}} \left(K_i - \frac{K_{i+1}}{N^2} \right) R_{\eta,N^{1-i}t}^{[i]} \sin(\Phi_{\eta,N^{-i}t}^{[i]} - \theta_{\eta,t}) dt + dB_{\eta,t}, \quad (4.9)$$

where we introduced the notation $\omega_{\eta}^{[i]} := \omega_{[\eta]_i}$.

Assuming that N is large compared to the values in $(K_i)_{i \in \mathbb{N}}$, we see from (4.9) that on time scale t , each 1-block population evolves under (4.5) simply according to a noisy mean-field Kuramoto model with a perturbation (coming from the influence of the oscillators outside the 1-block) that vanishes as $N \rightarrow \infty$. For a suitably chosen μ_0 with mean $\int_{\mathbb{R}} \omega \mu_0(d\omega) = 0$, we therefore may expect

$$d\theta_{\eta,t} = \omega_{\eta}^{[0]} dt + K_1 R_{\eta,t}^{[1]} \sin(\Phi_{\eta,0}^{[1]} - \theta_{\eta,t}) dt + dB_{\eta,t}, \quad N \rightarrow \infty, \quad (4.10)$$

for $\eta \in \Omega_N$ and $t \geq 0$, in which case each 1-block population reaches on time scale t an equilibrium¹ distributed around the stationary average phase of the block. On time scale Nt , however, the block averages on scale 1 are not stationary, and each is attracted to the stationary average phase of the 2-block it is part of with a strength depending on the value of K_2 .

To clarify this, we consider the example that $\mu_i = \delta_0$ for each $i \in \mathbb{N}_0$ and

$$K_i = \begin{cases} 3, & i = 1, 2, \\ 0, & i \geq 3. \end{cases} \quad (4.11)$$

Moreover, we take γ to be the uniform distribution on \mathbb{S} , so that the phase coherence in each block is initially equal to zero. In this case, simulations carried out for the system

¹We know from Chapter 3 that at least the non-disordered distribution and the Lorentzian distribution are suitable choices for μ_0 such that (4.10) reaches an equilibrium state for each $K_1 > 0$.

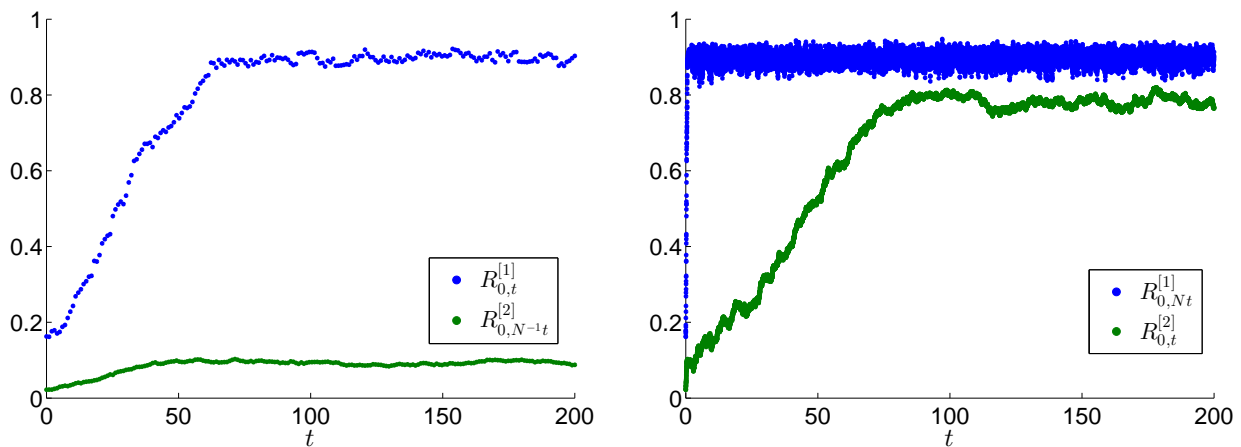


Figure 4.3: Simulation of the system given by (4.5) and (4.6), showing the evolution of the phase coherence in the 1-block and 2-block around the origin. Left: On time scale t , the 1-block population synchronizes and settles into a stationary state with $R^{[1]} > 0$, whereas the 2-block population as a whole remains in an incoherent state (the initial growth being a finite-size effect). Right: On time scale Nt , the 1-block immediately reaches equilibrium, and its average phase synchronizes with the other block averages on scale 1 in the 2-block such that the 2-block population settles into a stationary state with $0 < R^{[2]} < R^{[1]}$. These results are obtained with $N = 100$, γ the uniform distribution on \mathbb{S} , the coupling constants given by (4.11) and $\mu_i = \delta_0$ for each $i \in \mathbb{N}_0$. As numerical integration scheme the Milstein algorithm (see Appendix A) is used, and the corresponding Matlab code is provided in Section 4 of Appendix B.

given by (4.5) and (4.6) show that within each 1-block the oscillators reach on time scale t a state of equilibrium with a certain phase coherence $R^{[1]} > 0$ (see Figure 4.3a), just what we would expect from a noisy non-disordered mean-field Kuramoto model with a coupling above threshold $K_c = 1$ (see Section 3.5). The block averages on scale 1 are stationary on time scale t , but start to synchronize with the ones in the same 2-block on time scale Nt such that the oscillators in each 2-block settle into equilibrium with phase coherence $R^{[2]} > 0$ (see Figure 4.3b). Since each 1-block population on time scale Nt immediately reaches equilibrium with phase coherence $R^{[1]}$, we obtain from (4.7) that, roughly,

$$R_{\eta,t}^{[2]} = R^{[1]} \frac{1}{N} \sum_{\zeta \in B_2(\eta)/B_1(0)} e^{i(\Phi_{\zeta,t}^{[1]} - \Phi_{\eta,0}^{[2]})}, \quad \eta \in \Omega_N, t > 0, \quad (4.12)$$

where the index of the summation means that from each equivalence class in $B_2(\eta)/B_1(0)$ one representative ζ is taken. With (4.12) it becomes clear that $R^{[2]} \leq R^{[1]}$ when the 2-blocks are in equilibrium.

From the previous example we see that the chosen time scales in (4.7) are appropriate for our investigation of the synchronization behavior of the model. More generally, for a suitable choice of the law of disorder on each scale², we expect the following behavior of the model:

²We at least require, for each $k \in \mathbb{N}_0$, that μ_k is symmetric and unimodal around the zero frequency.

- (a) On time scale $N^k t$, the block averages on scale $> k$ are stationary, while the block averages on scale $k-1$ immediately reach an equilibrium with distribution $\nu^{[k]}$ on $\mathbb{S} \times \mathbb{R}$, so that $R^{[k]} = R^{[k-1]} \int_{\mathbb{S} \times \mathbb{R}} \cos(\varphi) d\nu^{[k]}(\varphi, \omega)$.
- (b) The block averages on scale k evolve on time scale $N^k t$ according to a noisy mean-field Kuramoto model with law of disorder μ_k and effective coupling depending on K_k and $\nu^{[k]}$, and reach an equilibrium with distribution $\nu^{[k+1]}$ on $\mathbb{S} \times \mathbb{R}$, so that $R^{[k+1]} = R^{[k]} \int_{\mathbb{S} \times \mathbb{R}} \cos(\varphi) d\nu^{[k+1]}(\varphi, \omega)$.
- (c) If the effective coupling on scale k is below a certain critical coupling, then $R^{[k+1]} = 0$. In that case, for each $i \in \mathbb{N}_0$ with $i \geq k$ the block averages on scale i settle on time scale $N^i t$ into an incoherent state with $R^{[i+1]} = 0$.

To verify this behavior rigorously, we need to develop a renormalization procedure for (4.5) in the hierarchical mean-field limit $N \rightarrow \infty$. To this end, we investigate in the next section how the block averages in (4.7) evolve under the process in (4.5).

4.4 Evolution of the block averages

To fix ideas, we assume from now on that the law of disorder on each scale is Lorentzian, meaning that for each $i \in \mathbb{N}_0$ the density of μ_i with respect to the Lebesgue measure is given by (2.22). Moreover, we fix an arbitrary $k \in \mathbb{N}$ and consider without loss of generality the evolution of the block average $\Phi_{0,t}^{[k]}$, which is the average phase of the oscillators in the k -block around the origin.

4.4.1 Exact results

From Ito's rule (A.17) follows that

$$d\Phi_{0,t}^{[k]} = \sum_{\zeta \in B_k(0)} \frac{\partial \Phi_0^{[k]}}{\partial \theta_\zeta} d\theta_{\zeta, N^k t} + \frac{1}{2} \sum_{\zeta \in B_k(0)} \frac{\partial^2 \Phi_0^{[k]}}{\partial \theta_\zeta^2} d(N^k t). \quad (4.13)$$

Furthermore, for $\Phi_{0,t}^{[k]} \in (-\pi, \pi)$ we have

$$\Phi_{0,t}^{[k]} = 2 \arctan \left(\frac{\sin \Phi_{0,t}^{[k]}}{1 + \cos \Phi_{0,t}^{[k]}} \right), \quad (4.14)$$

from which one, together with (4.7), can derive that

$$\frac{\partial \Phi_0^{[k]}}{\partial \theta_\zeta} = \frac{1}{N^k} \frac{1}{R_0^{[k]}} \cos(\Phi_0^{[k]} - \theta_\zeta), \quad \zeta \in B_k(0) \quad (4.15)$$

$$\frac{\partial^2 \Phi_0^{[k]}}{\partial \theta_\zeta^2} = -\frac{1}{N^{2k} (R_0^{[k]})^2} \sin(2(\Phi_0^{[k]} - \theta_\zeta)) + \frac{1}{N^k R_0^{[k]}} \sin(\Phi_0^{[k]} - \theta_\zeta), \quad \zeta \in B_k(0) \quad (4.16)$$

³The second marginal of $\nu^{[k]}(d\varphi, d\omega)$ is $\mu_k(d\omega)$, so that $\nu^{[k]}(d\varphi, d\omega) = \nu_\omega^{[k]}(d\varphi) \mu_k(d\omega)$ with $\nu_\omega^{[k]}$ a probability measure on \mathbb{S} for μ_k -a.e. ω .

Observe from (4.7) that

$$\sum_{\zeta \in B_k(0)} \sin(\Phi_{0,t}^{[k]} - \theta_{\zeta, N^{kt}}) = 0, \quad \zeta \in B_k(0), \quad (4.17)$$

so combining (4.9), (4.13), (4.15) and (4.16) gives

$$d\Phi_{0,t}^{[k]} = \sum_{i \in \mathbb{N}} \left(K_i - \frac{K_{i+1}}{N^2} \right) \frac{1}{R_{0,Nt}^{[k]}} \quad (4.18a)$$

$$\cdot \frac{1}{N^{i-1}} \left[\sum_{\zeta \in B_k(0)} R_{\zeta, N^{k-i+1}t}^{[i]} \sin(\Phi_{\zeta, N^{k-i}t}^{[i]} - \theta_{\zeta, N^{kt}}) \cos(\Phi_{0,t}^{[k]} - \theta_{\zeta, N^{kt}}) \right] dt \quad (4.18b)$$

$$- \frac{1}{2(R_{0,Nt}^{[k]})^2} \frac{1}{N^k} \sum_{\zeta \in B_k(0)} \sin(2(\Phi_{0,t}^{[k]} - \theta_{\zeta, N^{kt}})) dt \quad (4.18c)$$

$$+ \frac{1}{R_{0,Nt}^{[k]}} \sum_{i \in \mathbb{N}_0} \frac{1}{N^i} \left[\sum_{\zeta \in B_k(0)} \cos(\Phi_{0,t}^{[k]} - \theta_{\zeta, N^{kt}}) \omega_{\zeta}^{[i]} \right] dt \quad (4.18d)$$

$$+ \frac{1}{R_{0,Nt}^{[k]}} \frac{1}{N^{k/2}} \sum_{\zeta \in B_k(0)} \cos(\Phi_{0,t}^{[k]} - \theta_{\zeta, N^{kt}}) dB_{\zeta,t}. \quad (4.18e)$$

4.4.2 Expected behavior for $N \rightarrow \infty$

A rigorous analysis of (4.18) in the limit $N \rightarrow \infty$ needs to be done in order to develop a precise renormalization program for (4.5). The following results, however, are not exact, but we expect that these give a fair indication of the actual behavior of (4.18) for $N \rightarrow \infty$.

As discussed in Section 4.3, we expect that for each $i \in \mathbb{N}$ with $i \leq k-1$ the block averages on scale i immediately reach on time scale N^{kt} an equilibrium with distribution $\nu^{[i+1]}$ on $\mathbb{S} \times \mathbb{R}$, so that $R^{[i+1]} = R^{[i]} \int_{\mathbb{S} \times \mathbb{R}} \cos(\varphi) d\nu^{[i+1]}(\varphi, \omega)$. Since we think that these equilibria are obtained following the evolution of a noisy mean-field Kuramoto model, we expect in view of the results in Section 3.4 that each such distribution $\nu^{[i+1]}$ has a density $(\theta, \omega) \mapsto p^{[i+1]}(\theta, \omega)$ with respect to $\lambda \otimes \mu_{i+1}$ (with λ denoting the Lebesgue measure on \mathbb{S}) that satisfies the symmetry

$$p^{[i+1]}(\theta, \omega) = p^{[i+1]}(-\theta, -\omega), \quad \theta \in \mathbb{S}, \omega \in \text{supp}(\mu_i). \quad (4.19)$$

With (4.19), we expect that (4.18b) vanishes as $N \rightarrow \infty$ for each $i \in \mathbb{N}$ with $i \leq k$:

$$\frac{1}{N^{i-1}} \left[\sum_{\zeta \in B_k(0)} R_{\zeta, N^{k-i+1}t}^{[i]} \sin(\Phi_{\zeta, N^{k-i}t}^{[i]} - \theta_{\zeta, N^{kt}}) \cos(\Phi_{0,t}^{[k]} - \theta_{\zeta, N^{kt}}) \right] \rightarrow 0, \quad N \rightarrow \infty. \quad (4.20)$$

Moreover, observe that (4.20) is certainly true for $i \in \mathbb{N}$ with $i \geq k+2$, because the term between square brackets is always smaller than N^k .

Similarly, concerning (4.18d), we know that

$$\frac{1}{N^i} \left[\sum_{\zeta \in B_k(0)} \cos(\Phi_{0,t}^{[k]} - \theta_{\zeta, N^k t}) \omega_{\zeta}^{[i]} \right] \rightarrow 0, \quad N \rightarrow \infty \quad (4.21)$$

is true for $i \in \mathbb{N}_0$ with $i \geq k + 1$, and we think that (4.21) is also true for $i \in \mathbb{N}_0$ with $i \leq k - 1$ since μ_i is symmetric and (4.19) is expected.

Furthermore, applying (4.19) with $i = 1, \dots, k - 1$ to (4.18c) and (4.18e) gives

$$-\frac{1}{2(R_{0,Nt}^{[k]})^2} \frac{1}{N^k} \sum_{\zeta \in B_k(0)} \sin(2(\Phi_{0,t}^{[k]} - \theta_{\zeta, N^k t})) \rightarrow 0, \quad N \rightarrow \infty \quad (4.22)$$

and

$$\frac{1}{R_{0,Nt}^{[k]}} \frac{1}{N^{k/2}} \sum_{\zeta \in B_k(0)} \cos(\Phi_{0,t}^{[k]} - \theta_{\zeta, N^k t}) dB_{\zeta,t} \rightarrow \frac{\sqrt{Q^{[k]}}}{R^{[k]}} dB_{0,t}^{[k]}, \quad N \rightarrow \infty, \quad (4.23)$$

respectively. In (4.23), $B_0^{[k]}$ is a standard Brownian motion, and $Q^{[k]} \in [0, 1]$ is

$$Q^{[k]} = \lim_{N \rightarrow \infty} \frac{1}{N^k} \sum_{\zeta \in B_k(0)} \cos^2(\Phi_{0,t}^{[k]} - \theta_{\zeta, N^k t}), \quad (4.24)$$

which is a limit we expect to exist.

Applying (4.20) for each $i \in \mathbb{N} \setminus \{k + 1\}$, (4.21) for each $i \in \mathbb{N}_0 \setminus \{k\}$, (4.22) and (4.23) to (4.18), we obtain

$$\begin{aligned} d\Phi_{0,t}^{[k]} = & K_{k+1} \frac{R_{0,t}^{[k+1]}}{R^{[k]}} \left[\frac{1}{N^k} \sum_{\zeta \in B_k(0)} \sin(\Phi_{0,0}^{[k+1]} - \theta_{\zeta, N^k t}) \cos(\Phi_{0,t}^{[k]} - \theta_{\zeta, N^k t}) \right] dt \\ & + \omega_0^{[k]} dt + \frac{\sqrt{Q^{[k]}}}{R^{[k]}} dB_{0,t}^{[k]}, \quad N \rightarrow \infty. \end{aligned} \quad (4.25)$$

Moreover, the term in (4.25) between square brackets can be rewritten as follows:

$$\begin{aligned} & \frac{1}{N^k} \sum_{\zeta \in B_k(0)} \sin(\Phi_{0,0}^{[k+1]} - \theta_{\zeta, N^k t}) \cos(\Phi_{0,t}^{[k]} - \theta_{\zeta, N^k t}) \\ & = \frac{1}{2} \sin(\Phi_{0,0}^{[k+1]} - \Phi_{0,t}^{[k]}) - \frac{1}{2} \operatorname{Im} \left[e^{i(\Phi_{0,t}^{[k]} - \Phi_{0,0}^{[k+1]})} \frac{1}{N^k} \sum_{\zeta \in B_k(0)} e^{2i(\theta_{\zeta} - \Phi_{0,t}^{[k]})} \right] \\ & = \frac{1}{2} \sin(\Phi_{0,0}^{[k+1]} - \Phi_{0,t}^{[k]}) - \frac{1}{2} \operatorname{Im} \left[e^{i(\Phi_{0,t}^{[k]} - \Phi_{0,0}^{[k+1]})} \frac{1}{N^k} \sum_{\zeta \in B_k(0)} \cos(2(\theta_{\zeta} - \Phi_{0,t}^{[k]})) \right], \end{aligned} \quad (4.26)$$

where we applied (4.19) with $i = 1, \dots, k - 1$ in the last step. With (4.26), one can derive that (4.25) reduces to

$$d\Phi_{0,t}^{[k]} = K_{k+1} \frac{Q^{[k]}}{R^{[k]}} R_{0,t}^{[k+1]} \sin(\Phi_{0,0}^{[k+1]} - \Phi_{0,t}^{[k]}) dt + \omega_0^{[k]} dt + \frac{\sqrt{Q^{[k]}}}{R^{[k]}} dB_{0,t}^{[k]}, \quad N \rightarrow \infty. \quad (4.27)$$

Although (4.27) is not a precise result, it suggests that, in the hierarchical mean-field limit, $\Phi_{0,t}^{[k]}$ evolves according to a noisy mean-field Kuramoto model.

Appendix A

Numerical integration of stochastic differential equations (SDEs)

In this appendix we give some theoretical background for simulating stochastic differential equations (SDEs). We provide only some general ideas discussed in [20], and we refer to [20] and references therein for a more extensive study.

A.1 Informal interpretation of SDEs

Let us first consider stochastic differential equations on \mathbb{R} and with one-dimensional noise. The general form of such an SDE is

$$dX_t = \alpha(X_t, t)dt + \beta(X_t, t)dB_t, \quad (\text{A.1})$$

where α and β are known functions (called the *drift function* and *diffusion function*, respectively), and B denotes a standard Brownian motion (or Wiener process) on \mathbb{R} . Equation (A.1) should be understood as a shorthand notation for the integral equation

$$X_t = x + \int_{t_0}^t \alpha(X_s, s)ds + \int_{t_0}^t \beta(X_s, s)dB_s, \quad (\text{A.2})$$

where $x \in \mathbb{R}$ is the initial value of the stochastic process $\{X_t\}_{t \geq t_0}$. The second integral in the right-hand side of (A.2) is the so-called *Ito integral*, for which a precise definition can be found in e.g. [20]. Here we only give an informal interpretation of (A.1).

To this end, recall that the increments of the standard Brownian motion B are independent and normally distributed. More specifically, for $t_0 \leq s_1 < t_1 < s_2 < t_2$ we have that

$$B_{t_i} - B_{s_i} \sim \mathcal{N}(0, t_i - s_i), \quad i = 1, 2 \quad (\text{A.3})$$

and that $B_{t_1} - B_{s_1}$ and $B_{t_2} - B_{s_2}$ are independent. Hence, for each $t \geq t_0$, (A.1) indicates that X_t changes in an infinitesimal time increment dt by an amount $X_{t+dt} - X_t \sim \mathcal{N}(\alpha(X_t, t)dt, \beta(X_t, t)^2 dt)$ that is independent of the behavior of the process in $[t_0, t]$.

More generally, an SDE on \mathbb{R}^n with d -dimensional noise has the form

$$d\mathbf{X}_t = \boldsymbol{\alpha}(\mathbf{X}_t, t)dt + \boldsymbol{\beta}(\mathbf{X}_t, t)d\mathbf{B}_t, \quad (\text{A.4})$$

or, written in components,

$$dX_{i,t} = \alpha_i(\mathbf{X}_t, t)dt + \sum_{j=1}^d \beta_{ij}(\mathbf{X}_t, t)dB_{j,t}, \quad i = 1, \dots, n, \quad (\text{A.5})$$

where $\boldsymbol{\alpha}(\mathbf{X}_t, t) \in \mathbb{R}^n$, $\boldsymbol{\beta}(\mathbf{X}_t, t)$ is the $n \times d$ -matrix with entries $\beta_{ij}(\mathbf{X}_t, t) \in \mathbb{R}$ and $(B_i)_{i=1, \dots, d}$ are d i.i.d. standard Brownian motions. Again, (A.5) should be understood as a shorthand notation for the integral equations

$$X_{i,t} = x_i + \int_{t_0}^t \alpha_i(\mathbf{X}_s, s)ds + \sum_{j=1}^d \int_{t_0}^t \beta_{ij}(\mathbf{X}_s, s)dB_{j,s}, \quad i = 1, \dots, n, \quad (\text{A.6})$$

where $(x_1, \dots, x_n) \in \mathbb{R}^n$ is the initial value of the stochastic process $\{\mathbf{X}_t\}_{t \geq t_0}$. Again, in view of (A.3), an informal interpretation of (A.6) is that, for $t \geq t_0$, each $X_{i,t}$ changes in an infinitesimal time dt by an amount $X_{i,t+dt} - X_{i,t} \sim \mathcal{N}(\alpha_i(\mathbf{X}_t, t)dt, \sum_{j=1}^d \beta_{ij}(\mathbf{X}_t, t)^2 dt)$ that is independent of the behavior of the process in $[t_0, t]$.

We refer to [20] for precise conditions on the integrands in (A.2) and (A.6) required for the existence and uniqueness of solutions of the SDEs. For our purposes, we assume the general SDE (A.4) to be time-homogeneous, i.e. $\boldsymbol{\alpha}(\mathbf{X}_t, t) \equiv \boldsymbol{\alpha}(\mathbf{X}_t)$ and $\boldsymbol{\beta}(\mathbf{X}_t, t) \equiv \boldsymbol{\beta}(\mathbf{X}_t)$, with each α_i and β_{ij} twice-differentiable with respect to the components of \mathbf{X}_t . Under these assumptions, we will in the next section expand the integrals in (A.6), from which we can establish numerical integration schemes.

A.2 Ito-Taylor approximation

For simplicity, let us first consider the time-homogeneous version of (A.1), i.e.,

$$dX_t = \alpha(X_t)dt + \beta(X_t)dB_t, \quad (\text{A.7})$$

written in integral form as

$$X_t = X_{t_0} + \int_{t_0}^t \alpha(X_s)ds + \int_{t_0}^t \beta(X_s)dB_s. \quad (\text{A.8})$$

By expanding the integrals in (A.8) to a finite number of terms, we can obtain an approximation to the SDE (A.7) which becomes better as $\Delta t = t - t_0$ becomes smaller. For this, we first give a heuristic derivation of the one-dimensional *Ito rule*, which can

be seen as the stochastic counterpart of the one-dimensional chain rule in ordinary calculus.

To this end, let $f : \mathbb{R} \rightarrow \mathbb{R}$ be a smooth function of X_t . With a Taylor expansion, we obtain

$$df(X_t) = f(X_t + dX_t) - f(X_t) \quad (\text{A.9})$$

$$= f'(X_t)dX_t + \frac{1}{2}f''(X_t)(dX_t)^2 + \dots \quad (\text{A.10})$$

$$= f'(X_t)\{\alpha(X_t)dt + \beta(X_t)dB_t\} + \frac{1}{2}f''(X_t)\{\alpha(X_t)^2dt^2 + 2\alpha(X_t)\beta(X_t)dtdB_t + \beta(X_t)^2dB_t^2\} + \dots, \quad (\text{A.11})$$

where we have substituted for dX_t from (A.7). In ordinary calculus (i.e., $\beta(X_t) \equiv 0$), the second and higher terms in (A.10) become negligible compared to the first term as $dt \rightarrow 0$. However, in the stochastic situation (i.e., $\beta(X_t) \not\equiv 0$) this is not the case, since it turns out that $dB_t^2 = O(dt)$ for small dt . Intuitively speaking, this is because the Brownian motion B_t has relatively large fluctuations. Furthermore, for small dt we have $dtdB_t = O(dt^{3/2})$, so that from (A.11) we may write

$$df(X_t) = \left\{ \alpha(X_t)f'(X_t) + \frac{1}{2}\beta(X_t)^2f''(X_t) \right\} dt + \beta(X_t)f'(X_t)dB_t. \quad (\text{A.12})$$

This is the content of the one-dimensional Ito rule: Given a stochastic process $\{X_t\}_{t \geq t_0}$ on \mathbb{R} satisfying the SDE (A.7), for any twice-differentiable function $x \mapsto f(x)$ on \mathbb{R} the stochastic process $\{f(X_t)\}_{t \geq t_0}$ on \mathbb{R} satisfies the SDE (A.12), or written in integral form:

$$f(X_t) = f(X_{t_0}) + \int_{t_0}^t \left\{ \alpha(X_s)f'(X_s) + \frac{1}{2}\beta(X_s)^2f''(X_s) \right\} ds + \int_{t_0}^t \beta(X_s)f'(X_s)dB_s. \quad (\text{A.13})$$

A rigorous proof for the one-dimensional Ito rule (including its time-inhomogeneous version) can be found in e.g. [20].

Now, by applying Ito's rule to the twice-differentiable functions α and β in (A.8), one can derive the following Ito-Taylor approximation to the SDE (A.7):

$$X_t = X_{t_0} + \alpha(X_{t_0}) \int_{t_0}^t ds + \beta(X_{t_0}) \int_{t_0}^t dB_s + \beta(X_{t_0})\beta'(X_{t_0}) \int_{t_0}^t \left(\int_{t_0}^{s_1} dB_{s_2} \right) dB_{s_1}, \quad (\text{A.14})$$

where only terms up to first order in Δt are kept (see [20] for details).

Let us now turn to the time-homogeneous version of (A.4), i.e.,

$$d\mathbf{X}_t = \boldsymbol{\alpha}(\mathbf{X}_t)dt + \boldsymbol{\beta}(\mathbf{X}_t)d\mathbf{B}_t, \quad (\text{A.15})$$

written in integral form as

$$X_{i,t} = X_{i,t_0} + \int_{t_0}^t \alpha_i(\mathbf{X}_s) ds + \sum_{j=1}^d \int_{t_0}^t \beta_{ij}(\mathbf{X}_s) dB_{j,s}, \quad i = 1, \dots, n. \quad (\text{A.16})$$

In this more general setting, Ito's rule states that for any function $(x_1, \dots, x_n) \mapsto f(x_1, \dots, x_n)$ on \mathbb{R}^n which is twice differentiable w.r.t. each x_i , the stochastic process $\{f(\mathbf{X}_t)\}_{t \geq t_0}$ on \mathbb{R} satisfies

$$\begin{aligned} df(\mathbf{X}_t) = & \left\{ \sum_{i=1}^n \alpha_i(\mathbf{X}_t) \frac{\partial f}{\partial X_i}(\mathbf{X}_t) + \frac{1}{2} \sum_{i=1}^n \sum_{j=1}^d [\boldsymbol{\beta}(\mathbf{X}_t) \boldsymbol{\beta}^T(\mathbf{X}_t)]_{ij} \frac{\partial^2 f}{\partial X_i \partial X_j}(\mathbf{X}_t) \right\} dt \\ & + \sum_{i=1}^n \sum_{j=1}^d \beta_{ij}(\mathbf{X}_t) \frac{\partial f}{\partial X_i}(\mathbf{X}_t) dB_{j,s}, \end{aligned} \quad (\text{A.17})$$

or written in integral form:

$$\begin{aligned} f(\mathbf{X}_t) = & f(\mathbf{X}_{t_0}) + \sum_{i=1}^n \int_{t_0}^t \alpha_i(\mathbf{X}_s) \frac{\partial f}{\partial X_i}(\mathbf{X}_s) ds \\ & + \frac{1}{2} \sum_{i=1}^n \sum_{j=1}^d \int_{t_0}^t [\boldsymbol{\beta}(\mathbf{X}_s) \boldsymbol{\beta}^T(\mathbf{X}_s)]_{ij} \frac{\partial^2 f}{\partial X_i \partial X_j}(\mathbf{X}_s) ds \\ & + \sum_{i=1}^n \sum_{j=1}^d \int_{t_0}^t \beta_{ij}(\mathbf{X}_s) \frac{\partial f}{\partial X_i}(\mathbf{X}_s) dB_{j,s} \end{aligned} \quad (\text{A.18})$$

A heuristic derivation of this result can be given similar to the one for the one-dimensional case, and for a formal proof we refer again to [20]. By applying (A.18) to each α_i and β_{ij} in (A.16), one can derive the following Ito-Taylor approximation to the SDE (A.15):

$$\begin{aligned} X_{i,t} = & X_{i,t_0} + \alpha_i(\mathbf{X}_{t_0}) \int_{t_0}^t ds + \sum_{j=1}^d \beta_{ij}(\mathbf{X}_{t_0}) \int_{t_0}^t dB_{j,s} \\ & + \sum_{j,k=1}^d \sum_{l=1}^n \beta_{lk}(\mathbf{X}_{t_0}) \frac{\partial \beta_{ij}}{\partial X_l}(\mathbf{X}_{t_0}) \int_{t_0}^t \left(\int_{t_0}^{s_1} dB_{k,s_2} \right) dB_{j,s_1}, \quad i = 1, \dots, n, \end{aligned} \quad (\text{A.19})$$

where only terms up to first order in $\Delta t = t - t_0$ are kept (see [20] for details). Again, this approximation becomes better as Δt becomes smaller.

A.3 Numerical integration schemes

With (A.19) we are able to discuss two numerical integration schemes — the *Euler algorithm* and the *Milstein algorithm* — for the system

$$\begin{cases} d\mathbf{X}_t = \boldsymbol{\alpha}(\mathbf{X}_t) dt + \boldsymbol{\beta}(\mathbf{X}_t) d\mathbf{B}_t, & t \in [0, T], \\ \mathbf{X}_0 = \mathbf{x}. \end{cases} \quad (\text{A.20})$$

To this end, we divide the time interval $[0, T]$ into M subintervals of size $\Delta t = T/M$, separated from each other by the points $t_m = m\Delta t$ ($m = 0, 1, \dots, M$).

The Euler algorithm yields an approximated solution $\tilde{\mathbf{X}}^m$ for (A.20) at the points t_m by applying (A.19) with $t_0 = t_m$ and $t = t_{m+1}$ and neglecting the triple-sum term. More precisely, the algorithm uses as input the initial condition $\tilde{\mathbf{X}}^0 = \mathbf{x}$, and yields an approximated solution with the following iteration scheme:

For each $m = 0, 1, \dots, M - 1$ and each $i = 1, \dots, n$:

$$\tilde{X}_i^{m+1} = \tilde{X}_i^m + \alpha_i^m \Delta t + \sum_{j=1}^d \beta_{i,j}^m \Delta B_j^m, \quad (\text{A.21})$$

with

$$\alpha_i^m = \alpha_i(\tilde{\mathbf{X}}^m), \quad (\text{A.22})$$

$$\beta_{i,j}^m = \beta_{ij}(\tilde{\mathbf{X}}^m), \quad 1 \leq j \leq d, \quad (\text{A.23})$$

$$\Delta B_j^m = B_{j,t_{m+1}} - B_{j,t_m}, \quad 1 \leq j \leq d. \quad (\text{A.24})$$

On the other hand, the Milstein algorithm does not neglect the triple-sum term in (A.19), and yields an approximated solution $\tilde{\mathbf{X}}^m$ for (A.20) at the points t_m using the initial condition $\tilde{\mathbf{X}}^0 = \mathbf{x}$ and the following iteration scheme:

For each $m = 0, 1, \dots, M - 1$ and each $i = 1, \dots, n$:

$$\tilde{X}_i^{m+1} = \tilde{X}_i^m + \alpha_i^m \Delta t + \sum_{j=1}^d \beta_{i,j}^m \Delta B_j^m + \sum_{j,k=1}^d \gamma_{i,j,k}^m \Delta B_{j,k}^m, \quad (\text{A.25})$$

with

$$\alpha_i^m = \alpha_i(\tilde{\mathbf{X}}^m), \quad (\text{A.26})$$

$$\beta_{i,j}^m = \beta_{ij}(\tilde{\mathbf{X}}^m), \quad 1 \leq j \leq d, \quad (\text{A.27})$$

$$\Delta B_j^m = B_{j,t_{m+1}} - B_{j,t_m}, \quad 1 \leq j \leq d, \quad (\text{A.28})$$

$$\gamma_{i,j,k}^m = \sum_{l=1}^n \beta_{lk}(\tilde{\mathbf{X}}^m) \frac{\partial \beta_{ij}}{\partial X_l}(\tilde{\mathbf{X}}^m), \quad 1 \leq j, k \leq d, \quad (\text{A.29})$$

$$\Delta B_{j,k}^m = \int_{t_m}^{t_{m+1}} \left(\int_{t_m}^{s_1} dB_{k,s_2} \right) dB_{j,s_1}, \quad 1 \leq j, k \leq d. \quad (\text{A.30})$$

The accuracy of an algorithm such as the Euler and Milstein algorithm is typically expressed with the so-called *strong order of convergence* and *weak order of convergence*. The former is associated with the quantity

$$E_s(T) = \left(\mathbb{E}[(\tilde{X}_i^M - X_{i,T})^2] \right)^{1/2}, \quad (\text{A.31})$$

while the latter is associated with

$$E_{w,f}(T) = \mathbb{E}[f(\tilde{X}_i^M) - f(X_{i,T})], \quad (\text{A.32})$$

where f is a smooth function on \mathbb{R} .¹ The quantity $E_s(T)$ measures the root mean square of the difference between the solution of the algorithm and the exact solution of (A.20) after a time T . On the other hand, $E_{w,f}(T)$ quantifies the rate at which the exact mean of a smooth function f is approached by the one obtained from the algorithm. (With all feasible f , we obtain in this way a measure for the difference between the limiting distribution of the exact solution and the limiting distribution of the solution of the algorithm.)

For the Euler algorithm it is in [20] shown that $E_s(T) \sim \sqrt{\Delta t}$ and that $E_{w,f}(T) \sim \Delta t$ for all feasible f . In other words, the Euler algorithm has strong order of convergence $\sqrt{\Delta t}$, and weak order of convergence Δt . Furthermore, it is shown in [20] that the Milstein algorithm has both strong and weak order of convergence Δt , which indicates that the Milstein algorithm is more accurate than the Euler algorithm.

¹In (A.31) and (A.32) the average is taken over the index $i = 1, \dots, n$ and over different realizations of the Brownian motions.

Appendix B

Matlab code

In this appendix we provide the Matlab code that we used for the various simulations included in this thesis. We distinguish between simulations carried out for

- the mean-field Kuramoto model without noise (Section B.1), for which we use the Euler method for systems of ODEs (see e.g. [10], and note that this method coincides with the Euler algorithm discussed in Appendix A with zero diffusion matrix $\beta \equiv \mathbf{0}$),
- the noisy mean-field Kuramoto model (Section B.2), for which we use the Milstein algorithm discussed in Appendix A with unit diffusion matrix $\beta = I_N$ (note that in this case the Milstein algorithm and the Euler algorithm actually coincide),
- the Kuramoto-like model on the hierarchical lattice discussed in Chapter 4 (Section B.3), for which we use the Milstein algorithm discussed in Appendix A with unit diffusion matrix $\beta = I_N$ (again, in this case the Milstein algorithm and the Euler algorithm coincide).

B.1 Simulations in Chapter 2

Matlab code used for the simulation results displayed in Figure 2.2

```
1 N = 1000; %number of oscillators
2 dt = 0.05; %time increment
3 T = 1500; %time horizon
4 W = randn(N,1); %frequencies drawn from standard Gaussian
5 r = []; %declare array for values of r to be obtained
6 X0 = [zeros(N,1) ... %initialize phases to zero for K < Kc
7        rand(N,1)*2*pi]; %initialize phases uniformly for K > Kc
8
9 for K=1:2 %considered coupling strengths
10     X = X0(:,K); %choose corresponding initial distribution
11     for t = 1:T
```

```

12     real_part = 1/N*sum(arrayfun(@(y) cos(y),X)); %determine real part
13                                                     %of order parameter
14     imag_part = 1/N*sum(arrayfun(@(y) sin(y),X)); %determine imag part
15                                                     %of order parameter
16     r(K,t) = sqrt((real_part)^2+(imag_part)^2);
17     psi = 2*atan(imag_part/(r(K,t)+real_part));
18     A = arrayfun(@(x,y) K*r(K,t)*sin(psi-x)+y,X,W(:,1));
19     X = X + A*dt; %update X according to Euler method
20     end
21 end
22
23 figure
24 tsteps = linspace(0,T,T);
25 scatter(tsteps,r(1,1:T),3);
26 hold on;
27 scatter(tsteps,r(2,1:T),3);
28 axis([0,T,0,1])
29 xlabel('t')
30 ylabel('r')
31 legend('K < K_c','K > K_c')

```

Matlab code used for the simulation results displayed in Figure 2.3

```

1  N = 100; %number of oscillators (for (b), take N=1000)
2  dt = 0.05; %time increment
3  T = 2500; %time horizon
4  W = tan(pi*(rand(N,1)-0.5)); %frequencies distributed according to
5  %standard Lorentzian
6  dK = 0.16; %coupling strength increment
7  K = []; %declare array for values of K to be used
8  k = 51; %number of values of K to be used
9  r = []; %declare array for values of r to be obtained
10
11 for i = 1:k
12     K(i,1) = i*dK-dK; %coupling strengths run from 0 to 8
13     X = zeros(N,1); %initialize phases to zero
14     for t = 1:T
15         real_part = 1/N*sum(arrayfun(@(y) cos(y),X)); %determine real part
16                                                     %of order parameter
17         imag_part = 1/N*sum(arrayfun(@(y) sin(y),X)); %determine imag part
18                                                     %of order parameter
19         r(i,t) = sqrt((real_part)^2+(imag_part)^2);
20         psi = 2*atan(imag_part/(r(i,t)+real_part));
21         A = arrayfun(@(x,y) K(i,1)*r(i,t)*sin(psi-x)+y,X,W(:,1));
22         X = X + A*dt; %update X according to Euler method
23     end
24 end
25
26 figure
27 errorbar(K,mean(r(1:k,1500:2500)),2),std(r(1:k,1500:2500),0,2),'.k')
28 hold on;

```

```

29 km = @(x) sqrt(1-2/x);
30 fplot(km, [2, 8])
31 axis([0 8 0 1])
32 xlabel('K')
33 ylabel('r')

```

Matlab code used for the simulation results displayed in Figure 2.6

```

1 N = 2000; %number of oscillators
2 dt = 0.05; %time increment
3 T = 2500; %time horizon
4 W = rand(N,1)-1/2; %frequencies drawn from a uniform distribution
5 dK = 0.03; %coupling strength increment
6 K = []; %declare array for values of K to be used
7 k = 51; %number of values of K to be used
8 r = []; %declare array for values of r to be obtained
9
10 for i = 1:k
11     K(i,1) = i*dK-dK; %coupling strengths run from 0 to 1.5
12     X = zeros(N,1); %initialize phases to zero
13     for t = 1:T
14         real_part = 1/N*sum(arrayfun(@(y) cos(y),X)); %determine real part
15                                                     %of order parameter
16         imag_part = 1/N*sum(arrayfun(@(y) sin(y),X)); %determine imag part
17                                                     %of order parameter
18         r(i,t) = sqrt((real_part)^2+(imag_part)^2);
19         psi = 2*atan(imag_part/(r(i,t)+real_part));
20         A = arrayfun(@(x,y) K(i,1)*r(i,t)*sin(psi-x)+y,X,W(:,1));
21         X = X + A*dt; %update X according to Euler method
22     end
23 end
24
25 figure
26 errorbar(K,mean(r(1:k,1500:2500),2),std(r(1:k,1500:2500),0,2),'.k')
27 axis([0 1.5 0 1])
28 xlabel('K')
29 ylabel('r')

```

B.2 Simulations in Chapter 3

Matlab code used for the simulation results displayed in Figure 3.2

```

1 N = 100; %number of oscillators (for (b), take N=1000)
2 dt = 0.05; %time increment
3 T = 2500; %time horizon
4 W = tan(pi*(rand(N,1)-0.5)); %frequencies distributed according to
5 %standard Lorentzian
6 dK = 0.16; %coupling strength increment
7 K = []; %declare array for values of K to be used

```

```

8 k = 51; %number of values of K to be used
9 r = []; %declare array for values of r to be obtained
10
11 for i = 1:k
12     K(i,1) = i*dK-dK; %coupling strengths run from 0 to 8
13     X = zeros(N,1); %initialize phases to zero
14     for t = 1:T
15         real_part = 1/N*sum(arrayfun(@(y) cos(y),X)); %determine real part
16                                                     %of order parameter
17         imag_part = 1/N*sum(arrayfun(@(y) sin(y),X)); %determine imag part
18                                                     %of order parameter
19         r(i,t) = sqrt((real_part)^2+(imag_part)^2);
20         psi = 2*atan(imag_part/(r(i,t)+real_part));
21         A = arrayfun(@(x,y) K(i,1)*r(i,t)*sin(psi-x)+y,X,W(:,1));
22         B = randn(N,1);
23         X = X + A*dt+B*sqrt(dt); %update X according to Euler algorithm/
24                                 %Milstein algorithm
25     end
26 end
27
28 figure
29 errorbar(K,mean(r(1:k,1500:2500),2),std(r(1:k,1500:2500),0,2),'.k')
30 km = @(x) sqrt(1-3/x);
31 hold on;
32 fplot(km,[3,8])
33 axis([0 8 0 1])
34 xlabel('K')
35 ylabel('r')

```

B.3 Simulations in Chapter 4

Matlab code used for the simulation results displayed in Figure 4.3

```

1 N = 100; %number of oscillators
2 dt = 0.05; %time increment
3 T = 15000; %time horizon
4 K1 = 3; %coupling strength between pairs at distance 1
5 K2 = 3; %coupling strength between pairs at distance 2
6 R1 = []; %declare array for values of R1 to be obtained
7 R2 = []; %declare array for values of R2 to be obtained
8 X = rand(N*N,1)*2*pi; %initialize phases uniformly
9
10 for t = 1:T
11     real_part1 = []; %declare real part of 1-block order parameters
12     imag_part1 = []; %declare imag part of 1-block order parameters
13     Phi1 = [];
14     for i = 1:N
15         real_part1(i,1) = 1/N*sum(arrayfun(@(x) cos(x),X((i-1)*N+1:i*N,1)));
16         imag_part1(i,1) = 1/N*sum(arrayfun(@(x) sin(x),X((i-1)*N+1:i*N,1)));

```

```

17     R1(i,t) = sqrt((real_part1(i,1))^2+(imag_part1(i,1))^2);
18     Phi1(i,1) = 2*atan(imag_part1(i,1)/(R1(i,t)+real_part1(i,1)));
19     end
20     real_part2 = 1/N*sum(arrayfun(@(x,y) x*cos(y),R1(:,t),Phi1(:,1)));
21     imag_part2 = 1/N*sum(arrayfun(@(x,y) x*sin(y),R1(:,t),Phi1(:,1)));
22     R2(1,t) = sqrt((real_part2)^2+(imag_part2)^2);
23     Phi2 = 2*atan(imag_part2/(R2(1,t)+real_part2));
24     A = [];
25     for i = 1:N
26         A((i-1)*N+1:i*N,1) = arrayfun(@(x) (K1-K2/(N^2))*R1(i,t)*...
27             sin(Phi1(i,1)-x)+K2/N*R2(1,t)*sin(Phi2-x),X((i-1)*N+1:i*N,1));
28     end
29     B = randn(N*N,1);
30     X = X + A*dt + B*sqrt(dt);           %update X according to Euler algorithm/
31                                         %Milstein algorithm
32 end
33
34 figure
35 tsteps = linspace(0,T/N,T/N);
36 scatter(tsteps,R1(1,1:T/N),3);
37 hold on;
38 scatter(tsteps,R2(1,1:T/N),3);
39 axis([0,T/N,0,1])
40 xlabel('t')
41 legend('R^{[1]}','R^{[2]}')
42
43 figure
44 tsteps2 = linspace(0,T/N,T);
45 scatter(tsteps2,R1(1,1:T),3);
46 hold on;
47 scatter(tsteps2,R2(1,1:T),3);
48 axis([0,T/N,0,1])
49 xlabel('t')
50 legend('R^{[1]}','R^{[2]}')

```

Bibliography

- [1] J. A. Acebrón, L. L. Bonilla, C. J. Pérez Vicente, F. Ritort, and R. Spigler. The Kuramoto model: A simple paradigm for synchronization phenomena. *Reviews of Modern Physics*, 77(1):137–185, 2005.
- [2] A. Arenas, A. Díaz-Guilera, J. Kurths, Y. Moreno, and C. Zhou. Synchronization in complex networks. *Physics Reports*, 469(3):93–153, 2008.
- [3] A. Arenas, A. Diaz-Guilera, and C. J. Pérez-Vicente. Synchronization processes in complex networks. *Physica D: Nonlinear Phenomena*, 224(1):27–34, 2006.
- [4] A. Arenas, A. Díaz-Guilera, and C. J. Pérez-Vicente. Synchronization reveals topological scales in complex networks. *Physical Review Letters*, 96(11):114102, 2006.
- [5] J. T. Ariaratnam and S. H. Strogatz. Phase diagram for the winfree model of coupled nonlinear oscillators. *Physical Review Letters*, 86(19):4278–4281, 2001.
- [6] A. Barrat, M. Barthelemy, and A. Vespignani. *Dynamical processes on complex networks*. Cambridge University Press, 2008.
- [7] L. Bertini, G. Giacomin, and K. Pakdaman. Dynamical aspects of mean field plane rotators and the Kuramoto model. *Journal of Statistical Physics*, 138(1-3):270–290, 2010.
- [8] B. Bollobás. *Random graphs*. Springer, 1998.
- [9] L. L. Bonilla, J. C. Neu, and R. Spigler. Nonlinear stability of incoherence and collective synchronization in a population of coupled oscillators. *Journal of Statistical Physics*, 67(1-2):313–330, 1992.
- [10] J. C. Butcher. *Numerical methods for ordinary differential equations*. John Wiley & Sons, 2008.
- [11] R. Cohen and S. Havlin. Scale-free networks are ultrasmall. *Physical Review Letters*, 90(5):058701, 2003.
- [12] F. Collet. *The impact of disorder in the critical dynamics of mean-field models*. PhD thesis, Università degli studi di Padova, 2009.

-
- [13] L. da F. Costa, F. A. Rodrigues, G. Travieso, and P. R. Villas Boas. Characterization of complex networks: A survey of measurements. *Advances in Physics*, 56(1):167–242, 2007.
- [14] J. D. Crawford. Amplitude expansions for instabilities in populations of globally-coupled oscillators. *Journal of Statistical Physics*, 74(5-6):1047–1084, 1994.
- [15] P. Dai Pra and F. den Hollander. McKean-Vlasov limit for interacting random processes in random media. Technical report, Department of Mathematics, University of Nijmegen, 1995.
- [16] P. Dai Pra and F. den Hollander. McKean-Vlasov limit for interacting random processes in random media. *Journal of Statistical Physics*, 84(3-4):735–772, 1996.
- [17] H. Daido. Lower critical dimension for populations of oscillators with randomly distributed frequencies: a renormalization-group analysis. *Physical Review Letters*, 61(2):231, 1988.
- [18] H. Daido. Intrinsic fluctuation and its critical scaling in a class of populations of oscillators with distributed frequencies. *Progress of Theoretical Physics*, 81(4):727–731, 1989.
- [19] G. Filatrella, A. H. Nielsen, and N. F. Pedersen. Analysis of a power grid using a Kuramoto-like model. *The European Physical Journal B*, 61(4):485–491, 2008.
- [20] C. W. Gardiner. *Stochastic methods: A handbook for the natural and social sciences*. Springer, Berlin, 2009.
- [21] G. Giacomin, K. Pakdaman, and X. Pellegrin. Global attractor and asymptotic dynamics in the Kuramoto model for coupled noisy phase oscillators. *Nonlinearity*, 25(5):1247–1273, 2012.
- [22] J. Gómez-Gardeñes, Y. Moreno, and A. Arenas. Paths to synchronization on complex networks. *Physical Review Letters*, 98(3):034101, 2007.
- [23] J. Gómez-Gardeñes, Y. Moreno, and A. Arenas. Synchronizability determined by coupling strengths and topology on complex networks. *Physical Review E*, 75(6):066106, 2007.
- [24] A. Greven, F. den Hollander, and A. Klimovsky. The hierarchical Cannings process in random environment. In preparation.
- [25] F. den Hollander. *Large deviations*. Fields Institute Monographs. American Mathematical Society, Providence, RI, 2000.
- [26] F. den Hollander. Renormalization of interacting diffusions: a program and four examples. In E. Koelink, J. M. A. M. van Neerven, B. de Pagter, and G. H. Sweers, editors, *Partial differential equations and functional analysis: the Philippe Clément festschrift*, volume 168, pages 123–136. Springer Science & Business Media, 2006.

-
- [27] H. Hong, M. Y. Choi, and B. J. Kim. Synchronization on small-world networks. *Physical Review E*, 65(2):026139, 2002.
- [28] T. Ichinomiya. Frequency synchronization in a random oscillator network. *Physical Review E*, 70(2):026116, 2004.
- [29] S. Y. Kourtchatov, V. V. Likhanskii, A. P. Napartovich, F. T. Arecchi, and A. Lapucci. Theory of phase locking of globally coupled laser arrays. *Physical Review A*, 52(5):4089, 1995.
- [30] Y. Kuramoto. Self-entrainment of a population of coupled non-linear oscillators. In *International Symposium on Mathematical Problems in Theoretical Physics*, pages 420–422. Lecture Notes in Phys., 39. Springer, Berlin, 1975.
- [31] Y. Kuramoto. *Chemical oscillations, waves, and turbulence*. Springer-Verlag, New York, 1984.
- [32] D. S. Lee. Synchronization transition in scale-free networks: Clusters of synchrony. *Physical Review E*, 72(2):026208, 2005.
- [33] E. Luçon. Quenched limits and fluctuations of the empirical measure for plane rotators in random media. *Electronic Journal of Probability*, 16:792–829, 2011.
- [34] E. Luçon. *Oscillateurs couplés, désordre et synchronisation*. PhD thesis, Université Pierre et Marie Curie-Paris VI, 2012.
- [35] E. A. Martens, E. Barreto, S. H. Strogatz, E. Ott, P. So, and T. M. Antonsen. Exact results for the Kuramoto model with a bimodal frequency distribution. *Physical Review E*, 79(2):026204, 2009.
- [36] D. C. Michaels, E. P. Matyas, and J. Jalife. Mechanisms of sinoatrial pacemaker synchronization: a new hypothesis. *Circulation Research*, 61(5):704–714, 1987.
- [37] J. Pantaleone. Stability of incoherence in an isotropic gas of oscillating neutrinos. *Physical Review D*, 58(7):073002, 1998.
- [38] D. Pazó. Thermodynamic limit of the first-order phase transition in the Kuramoto model. *Physical Review E*, 72(4):046211, 2005.
- [39] C. S. Peskin. *Mathematical aspects of heart physiology*. Courant Institute of Mathematical Sciences, New York University, 1975.
- [40] H. Sakaguchi. Cooperative phenomena in coupled oscillator systems under external fields. *Progress of Theoretical Physics*, 79(1):39–46, 1988.
- [41] S. H. Strogatz. Spontaneous synchronization in nature. In *IEEE International Frequency Control Symposium*, pages 2–4. New York, 1997.
- [42] S. H. Strogatz. From Kuramoto to Crawford: exploring the onset of synchronization in populations of coupled oscillators. *Physica D: Nonlinear Phenomena*, 143(1):1–20, 2000.

- [43] S. H. Strogatz. Exploring complex networks. *Nature*, 410(6825):268–276, 2001.
- [44] S. H. Strogatz. *Sync: The emerging science of spontaneous order*. Hyperion, 2003.
- [45] S. H. Strogatz and R. E. Mirollo. Collective synchronisation in lattices of nonlinear oscillators with randomness. *Journal of Physics A: Mathematical and General*, 21(13):L699–L705, 1988.
- [46] S. H. Strogatz and R. E. Mirollo. Phase-locking and critical phenomena in lattices of coupled nonlinear oscillators with random intrinsic frequencies. *Physica D: Nonlinear Phenomena*, 31(2):143–168, 1988.
- [47] S. H. Strogatz and R. E. Mirollo. Stability of incoherence in a population of coupled oscillators. *Journal of Statistical Physics*, 63(3-4):613–635, 1991.
- [48] H. A. Tanaka, A. J. Lichtenberg, and S. Oishi. Self-synchronization of coupled oscillators with hysteretic responses. *Physica D: Nonlinear Phenomena*, 100(3):279–300, 1997.
- [49] J. L. Van Hemmen and W. F. Wreszinski. Lyapunov function for the Kuramoto model of nonlinearly coupled oscillators. *Journal of Statistical Physics*, 72(1-2):145–166, 1993.
- [50] Y. M. Vega, M. Vázquez-Prada, and A. F. Pacheco. Fitness for synchronization of network motifs. *Physica A: Statistical Mechanics and its Applications*, 343:279–287, 2004.
- [51] T. J. Walker. Acoustic synchrony: two mechanisms in the snowy tree cricket. *Science*, 166(3907):891–894, 1969.
- [52] D. J. Watts and S. H. Strogatz. Collective dynamics of ‘small-world’ networks. *Nature*, 393(6684):440–442, 1998.
- [53] K. Wiesenfeld, P. Colet, and S. H. Strogatz. Synchronization transitions in a disordered Josephson series array. *Physical Review Letters*, 76:404–407, 1996.
- [54] K. Wiesenfeld, P. Colet, and S. H. Strogatz. Frequency locking in Josephson arrays: connection with the Kuramoto model. *Physical Review E*, 57(2):1563, 1998.
- [55] A. T. Winfree. Biological rhythms and the behavior of populations of coupled oscillators. *Journal of Theoretical Biology*, 16(1):15–42, 1967.
- [56] A. T. Winfree. *The geometry of biological time*. Springer, New York, 1980.
- [57] R. York and R. C. Compton. Quasi-optical power combining using mutually synchronized oscillator arrays. *Microwave Theory and Techniques, IEEE Transactions on* 39(6) : 1000–1009, 1991.
- [58] X. Zhang, S. Boccaletti, S. Guan, and Z. Liu. Explosive synchronization in adaptive and multilayer networks. *Physical Review Letters*, 114(3):038701, 2015.